RESEARCH ARTICLE

Distinct Assemblies of Heterodimeric Cytokine Receptors Govern Stemness Programs in Leukemia

Winnie L. Kan[1], Urmi Dhagat[2,3], Kerstin B. Kaufmann[4], Timothy R. Hercus[1], Tracy L. Nero[2,3], Andy G.X. Zeng[4,5], John Toubia[6], Emma F. Barry[1], Sophie E. Broughton[2,3], Guillermo A. Gomez[6], Brooks A. Benard[7], Mara Dottore[1], Karen S. Cheung Tung Shing[2,3], Héléna Boutzen[4], Saumya E. Samaraweera[6], Kaylene J. Simpson[8,9], Liqing Jin[4], Gregory J. Goodall[6,10], C. Glenn Begley[11], Daniel Thomas[7,10], Paul G. Ekert[12,13,14], Denis Tvorogov[1], Richard J. D'Andrea[6], John E. Dick[4,5], Michael W. Parker[2,3], and Angel F. Lopez[1,10]

ABSTRACT Leukemia stem cells (LSC) possess distinct self-renewal and arrested differentiation properties that are responsible for disease emergence, therapy failure, and recurrence in acute myeloid leukemia (AML). Despite AML displaying extensive biological and clinical heterogeneity, LSC with high interleukin-3 receptor (IL3R) levels are a constant yet puzzling feature, as this receptor lacks tyrosine kinase activity. Here, we show that the heterodimeric IL3Rα/βc receptor assembles into hexamers and dodecamers through a unique interface in the 3D structure, where high IL3Rα/βc ratios bias hexamer formation. Importantly, receptor stoichiometry is clinically relevant as it varies across the individual cells in the AML hierarchy, in which high IL3Rα/βc ratios in LSCs drive hexamer-mediated stemness programs and poor patient survival, while low ratios mediate differentiation. Our study establishes a new paradigm in which alternative cytokine receptor stoichiometries differentially regulate cell fate, a signaling mechanism that may be generalizable to other transformed cellular hierarchies and of potential therapeutic significance.

SIGNIFICANCE: Stemness is a hallmark of many cancers and is largely responsible for disease emergence, progression, and relapse. Our finding that clinically significant stemness programs in AML are directly regulated by different stoichiometries of cytokine receptors represents a hitherto unexplained mechanism underlying cell-fate decisions in cancer stem cell hierarchies.

INTRODUCTION

Normal and malignant hematopoiesis are organized in a cellular hierarchy with rare stem cells at the apex that both self-renew and differentiate into all mature blood lineages (1, 2). This balance between stemness and commitment is regulated by interleukin (IL) 3 and other pleiotropic cytokines (3); however, how they determine cell fate remains a mystery. Cytokine-mediated dimerization of receptor subunits provides one mechanism that explains pleiotropy arising through the combined effects of binding affinities and kinetics, and stability and topology of complex formation (4–7). These concepts led to the development of newly engineered ligands of erythropoietin (EPO; ref. 6), stem cell factor (SCF; ref. 8), IL2 (9, 10), and interferon (IFN; ref. 11) to stimulate differential qualitative signaling, with engineered IL2 partial agonists recently entering phase Ia/Ib clinical trials for treatment of advanced solid tumors (NCT05098132; ref. 12). However, some type I cytokine receptors such as those for growth hormone and granulocyte–macrophage colony-stimulating factor (GM-CSF) can exist in different oligomerization states (13, 14), pointing to variation in oligomerization as an unappreciated alternative possibility for functional pleiotropism.

IL3 stimulates fate outcomes including survival, expansion, and differentiation across many individual cell types that make up the hematopoietic hierarchy (3, 15). IL3 engages a single heterodimeric receptor (IL3R) comprising a cytokine-specific α-subunit (IL3Rα, *IL3RA*, and CD123) and a shared signaling subunit (βc, *CSF2RB*, CD131) that, when dimerized, will activate the JAK–STAT, PI3K–AKT and RAS–MAPK pathways (15). The IL3R system is of particular significance for the cellular hierarchies found in leukemia because the

[1]Cytokine Receptor Laboratory, Centre for Cancer Biology, SA Pathology and the University of South Australia, Adelaide, South Australia, Australia. [2]Australian Cancer Research Foundation Rational Drug Discovery Centre, St. Vincent's Institute of Medical Research, Fitzroy, Victoria, Australia. [3]Department of Biochemistry and Pharmacology and the Australian Cancer Research Foundation Facility for Innovative Cancer Drug Discovery, Bio21 Molecular Science and Biotechnology Institute, University of Melbourne, Parkville, Victoria, Australia. [4]Princess Margaret Cancer Centre, University Health Network, Toronto, Ontario, Canada. [5]Department of Molecular Genetics, University of Toronto, Toronto, Ontario, Canada. [6]Centre for Cancer Biology, SA Pathology and the University of South Australia, Adelaide, South Australia, Australia. [7]Division of Hematology, Department of Medicine, Cancer Institute, and Institute for Stem Cell Biology and Regenerative Medicine, Stanford University School of Medicine, Stanford, California. [8]Victorian Centre for Functional Genomics, Peter MacCallum Cancer Centre, Melbourne, Victoria, Australia. [9]The Sir Peter MacCallum Department of Oncology, University of Melbourne, Parkville, Victoria, Australia. [10]Department of Medicine, University of Adelaide, Adelaide, South Australia, Australia. [11]Begley Biotech Consulting, Wallington, Victoria, Australia. [12]Translational Tumour Biology Group, Children's Cancer Institute, Lowy Cancer Centre, University of New South Wales, Randwick, New South Wales, Australia. [13]Cancer Research Division, Peter MacCallum Cancer Centre, Melbourne, Victoria, Australia. [14]Cancer Research, Murdoch Children's Research Institute, Royal Children's Hospital, Parkville, Victoria, Australia.

Note: W.L. Kan, U. Dhagat, K.B. Kaufmann, and T.R. Hercus contributed equally to this article.

T.L. Nero, A.G.X. Zeng, and J. Toubia contributed equally to this article.

Corresponding Authors: Angel F. Lopez, Cytokine Receptor Laboratory, Centre for Cancer Biology, PO Box 14 Rundle Mall, Adelaide, South Australia 5000, Australia. Phone: 61-8-8302-7916; Fax: 61-8-8302-9246; E-mail: Angel.Lopez@sa.gov.au; Michael W. Parker, Bio21 Molecular Science and Biotechnology Institute (Bio21 Institute), 30 Flemington Road, Parkville, Victoria 3010, Australia. Phone: 61-3-8344-2211; Fax: 61-3-9416-2676; E-mail: mparker@svi.edu.au; and John E. Dick, Princess Margaret Cancer Centre, University Health Network, Princess Margaret Cancer Research Tower, 8th Floor, Room 8-358, 101 College Street, Toronto, Ontario, M5G 1L7, Canada. Phone: 416-581-7472; E-mail: John.Dick@uhnresearch.ca

Cancer Discov 2023;13:1922–47

doi: 10.1158/2159-8290.CD-22-1396

IL3Rα subunit is selectively upregulated both on leukemia stem cells (LSC) and myeloid blasts in 90% of patients with acute myeloid leukemia (AML) and is associated with clinical features including elevated blast count at presentation, poor prognosis, and lower rates of complete remission (16–19). LSCs are clinically relevant, as they are responsible for disease emergence, therapy failure, and disease recurrence, and their stemness program predicts poor patient survival (20, 21). Puzzlingly, LSCs with high IL3Rα levels (16) represent a common feature across a diverse range of patients with AML who are otherwise highly biologically and clinically heterogeneous. Unlike several upregulated receptors in other cancers (22), the IL3R heterodimer lacks intrinsic tyrosine kinase activity (23). This raises a fundamental question of how the upregulation of a single, non–tyrosine kinase receptor subunit can affect receptor assembly, quality of signaling, and, ultimately, the biology of cancer "stemness."

RESULTS

Discordant IL3Rα and βc Expression Is Associated with Stemness and Poor Patient Survival in AML

Receptor-mediated oncogenesis, for example, by tyrosine kinases such as HER2 in breast cancer (24), has been classically ascribed to receptor overexpression leading to excessive signaling. However, analysis of the subunits of IL3R revealed that patients with AML with high IL3Rα gene expression unexpectedly expressed low βc gene expression and vice versa (Fig. 1A; Supplementary Fig. S1A), contradicting this general assumption and hinting of an alternative stoichiometry. Across a continuum of IL3Rα/βc gene expression ratios, we performed the log-rank statistical analysis to determine a ratio cutoff of 1.1 for IL3Rα/βc that gave the highest hazard ratio (HR) for decreased overall survival. We found that a high ratio (IL3Rα>βc) was consistently associated with worse patient survival across two normal karyotype patient cohorts (refs. 25, 26; Fig. 1B; Supplementary Fig. S1B), and our multivariate meta-analyses across five patient cohorts (25–28) revealed that higher IL3Rα/βc gene expression ratios were an independent predictor of worse patient survival (combined $P = 0.0091$; Supplementary Fig. S1C). This result was specific to IL3Rα/βc ratios, as there was no difference in overall survival between transcript ratios of other heterodimeric cytokine receptors (Supplementary Fig. S1D and S1E). Of note, high IL3Rα/βc ratios were observed in patients with AML (25, 26) carrying somatic driver *FLT3* internal tandem duplication (*FLT3*-ITD) and *RUNX1* mutations (Supplementary Fig. S1F), which are associated with poor prognosis (29, 30) and primitive cellular hierarchy and stemness signatures (31), using the recently reported hierarchy-classification system (32). Conversely, low ratios were seen in patients with *NRAS* or *KRAS* mutations (Supplementary Fig. S1F), which are associated with a differentiated hierarchy and are more responsive to chemotherapy (31, 33).

Given the strong link between stemness and poor survival in AML (20, 34), we grouped patient samples from the Beat AML cohort into high- and low-ratio quartiles and performed gene set enrichment analysis (GSEA), and found that a high IL3Rα/βc ratio is associated with a stem/progenitor-like transcriptional state (Supplementary Fig. S1G; ref. 26). Next, we interrogated recent single-cell and functionally validated LSC transcriptomic datasets for IL3Rα and βc expression (20, 21, 35). This revealed that the IL3Rα/βc ratio is higher and closely associated with leukemia stem and progenitor cell quiescent (LSPC-quiescent) and primed (LSPC-primed) transcriptional phenotypes (32), in contrast to committed myeloid-like blast phenotypes [granulocyte-monocyte progenitor (GMP)–like, ProMonocyte (ProMono)-like, and Monocyte (Mono)-like; ref. 35; Fig. 1C]. For eight of 10 primary AML samples from the Toronto cohort, combined immunophenotypic and transcriptional profiling resulted in clustering of high-ratio samples to a more primitive phenotype cluster (defined by high %$CD34^+CD38^-$ and LSPC-quiescent signature enrichment) and low-ratio samples to a more mature phenotypic cluster (high %$CD36^+$, Mono-like signature; Fig. 1D). Similarly, our analysis of the IL3Rα/βc gene expression ratio in highly purified and functionally validated immunophenotypic fractions from human umbilical cord blood (CB; refs. 36, 37) revealed that the ratio was also higher in normal stem and myeloid progenitor cells compared with differentiated monocytic cells (Fig. 1E). We performed cell-surface analysis of the IL3Rα/βc protein ratio in 21 primary AML patient samples from two independent cohorts in Toronto and Adelaide that were selected for high versus low IL3Rα/βc

Figure 1. Divergent IL3Rα and βc expression preferentially occurs at the apex of the hematopoietic cell hierarchy and is linked to poor patient survival in AML. **A,** IL3Rα and βc gene expression ratio in 451 *de novo* normal karyotype patients with AML, as shown in reads per kilobase per million mapped reads (RPKM; Beat AML; ref. 26). Av, average. **B,** Kaplan–Meier overall survival curve for normal karyotype patients with AML comparing those with higher or lower than 1.1 ratio of IL3Rα/βc expression in The Cancer Genome Atlas cohort ($n = 184$; ref. 25). **C,** Single-cell gene expression of IL3Rα and βc across 11,641 single AML cells from 12 patients (35), with cell types annotated from (32). Mean gene expression is depicted for each AML cell type. **D,** Hierarchical clustering of primary AML patient samples with high ($n = 5$) and low ($n = 5$) IL3Rα/βc ratio [RNA sequencing (RNA-seq)] combining transcriptional (*; RNA-seq) and immunophenotypic (flow cytometry) profiling in the Toronto cohort. **E,** IL3Rα and βc gene expression in sorted and functionally validated immunophenotypic cellular fractions from CB (36, 37). CMP, common myeloid progenitors; GMP, granulocyte-monocyte progenitors; Gr, granulocytes; HSC, hematopoietic stem cells; MEP, megakaryocyte-erythroid progenitors; MLP, multilymphoid progenitors; Mono, monocytes; MPP, multipotent progenitors. **F,** Flow cytometric analysis for %$IL3R\alpha^{hi}\beta c^{lo}$ population of high ($n = 5$, blue) and low ($n = 5$, red) IL3Rα/βc transcript ratio AML patient samples ($CD3^-CD19^-CD45^+$) in the Toronto cohort based on cell-surface IL3Rα and βc protein expression profiles. CB mononuclear cells ($n = 3$) and mobilized peripheral blood (mPB) mononuclear cells ($n = 1$) served as controls (ctrl). ns, not significant. **G,** Correlation of relative abundance of cells with quiescent and primed combined transcriptional phenotypes with %$IL3R\alpha^{hi}/\beta c^{lo}$ population in $CD3^-CD19^-CD45^+$ cells with high and low IL3Rα/βc ratio (by RNA-seq) in the Toronto cohort by Pearson analysis. **H,** Spearman correlation between gene expression and LSC frequency from 88 AML fractions in which specific LSC frequencies were calculated by limiting dilution analysis (LDA) in xenograft assays (20, 38). IL3Rα (*IL3RA*) and βc (*CSF2RB*) are highlighted. **I,** IL3Rα/βc transcript ratio from 138 LSC^+ (engrafting) and 82 LSC^- (nonengrafting) fractions (20). **J,** Sorting gates for xenotransplanted high/medium (med)/low IL3Rα/βc ratio (CD123 vs. CD131) fractions for patient sample AML#140005 and AML#130578 are shown pregated for viable ($SytoxBlue^-$) and $CD45^+CD3^-CD19^-$ cells and in relation to an in parallel stained G-CSF mobilized peripheral blood control sample (mPB ctrl) from a healthy donor. **K,** LSC frequencies of high/med/low IL3Rα/βc ratio fractions from AML#140005 and AML#130578 xenotransplanted in limiting dilution into NSG-SGM3 and NSG mice as estimated from $CD45^+CD33^+$ engraftment (>0.1%) at 7 to 8 weeks after transplantation (see also Supplementary Fig. S1Q). Due to low cell numbers retrieved, the low-ratio fraction of AML#130578 was transplanted only into NSG-SGM3. Open triangle and dotted error bar line indicate an estimated 1/LSC frequency and upper limit of 1. Upper and lower estimated limit (error bars) and *P* values as calculated by ELDA.

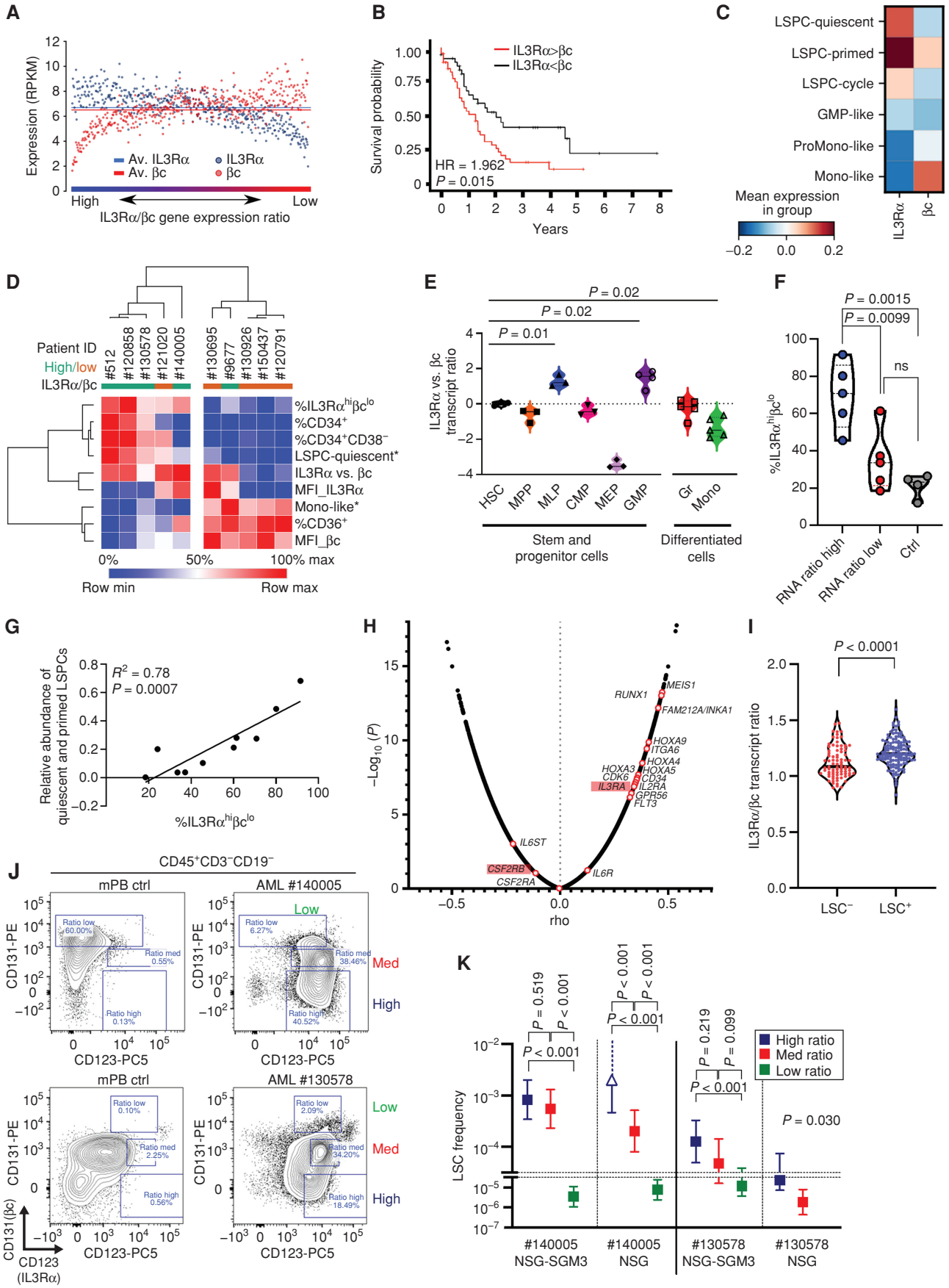

transcript ratios. AML patient samples with a high transcript ratio also had a higher abundance of an IL3Rα^{hi}βc^{lo} population and higher overall IL3Rα/βc protein ratio (Fig. 1F; Supplementary Fig. S1H–S1K), which is found in the CD34^{+} fraction (Supplementary Fig. S1L and S1M). Furthermore, the proportion of IL3Rα^{hi}βc^{lo} cells strongly correlated with the relative abundance of cells with quiescent and primed LSPC transcriptional phenotypes, contrasting with a negative correlation for the Mono-like blast state (Fig. 1G; Supplementary Fig. S1N–S1P; Toronto cohort). To more closely link high IL3Rα/βc transcript ratios with LSC activity, Spearman analysis of LSC frequency based on limiting dilution xenografting of primary AMLs with gene expression showed a statistically significant positive correlation for IL3Rα (*IL3RA*; Fig. 1H; rho = 0.342; $P = 1.29E{-}07$; rank 624 of 30,460 genes; refs. 20, 38), similar to other genes associated with hematopoietic and leukemia stem and progenitor cells (*CD34*, *GPR56*, and *FLT3*; refs. 1, 2, 20, 34, 39), while no correlation was observed for βc (*CSF2RB;* rho = –0.113; $P = 0.09$; rank 25,340/30,460). The high IL3Rα/βc transcript ratios calculated for LSC-positive (engrafting) in contrast to non-LSC (nonengrafting) fractions (ref. 20; Fig. 1I) lend further credence to the functional relevance of discordant receptor subunit expression in primary AML samples. To link the IL3Rα/βc surface ratio directly to LSC frequency, we isolated high, medium (med), and low IL3Rα/βc ratio fractions from two high IL3Rα/βc transcript ratio AML samples (Toronto cohort #130578 and #140005) and tested LSC frequency using a limiting dilution assay (LDA) approach in NSG and human IL3-expressing NSG-SGM3 mice (Fig. 1J). LSC frequencies showed a gradient from high>med>low ratio fractions and were 10- to 240-fold higher in the IL3Rα/βc ratio–high versus –low fractions, depending on the AML sample and mouse model used (Fig. 1K; Supplementary Fig. S1Q). These data indicated that both protein and transcript ratios of IL3Rα versus βc, and ultimately the resulting stoichiometry, play a role in regulating and determining stemness and prognosis in AML.

The IL3 Heterodimeric Receptor Exhibits Two Distinct Forms of Assembly

To understand how the arrangement of IL3R subunits influences stemness and outcomes in AML, we undertook a detailed structural analysis of the heterodimeric receptor complex. The crystal structure of the ternary IL3R complex, comprising IL3 bound to the extracellular domains of the IL3Rα and βc subunits (Fig. 2A and B), was determined to 3.3 Å resolution (data collection and refinement statistics are summarized in Supplementary Table S1). The assembly of IL3, IL3Rα, and βc in the asymmetric unit consists of two partial hexameric complexes placed adjacent to each other such that the complete assembly forms a dodecamer composed of two hexamer complexes in a head-to-head arrangement (Fig. 2A and B). Assembly of the hexameric complex occurs via sites 1 to 3 (Fig. 2A and B; Supplementary Table S2), with IL3 binding to IL3Rα through site 1a/1b and to βc through site 2, while the interaction between the membrane-proximal domains of IL3Rα and βc occurs via site 3 (Fig. 2A and B; Supplementary Fig. S2A and S2B). Assembly of the dodecamer arises from adjacent hexamers and involves interactions between distinct residues in the membrane proximal domains of IL3Rα and βc (Fig. 2C) that represent an "assembly interface," and from IL3–IL3' interactions between the adjacent hexamers (Supplementary Fig. S2C and S2D). The "assembly interface" is formed by the side chains of Q243', M246,' P248', and V249' from IL3Rα' domain (D)3 and Q346, T348, and K349 from βc D4 (Fig. 2C) and, likewise, Q243, M246, P248, and V249 from IL3Rα D3 and Q346,' T348', and K349' from βc' D4. Hence, the IL3R dodecameric assembly is strongly contrasting to the GM-CSF receptor dodecamer, which is largely a βc–βc' interaction (Supplementary Fig. S2E) that functionally dimerizes the βc cytoplasmic domains (Fig. 2C), allowing transactivation of βc-associated JAK molecules (13, 40, 41).

Solving the structure of the ternary IL3R complex enabled us to dissect the biological and signaling differences between the IL3R hexamer and dodecamer configurations by judiciously disrupting the "assembly interface." Our analysis of the structure suggested T348, K349, and G351 of βc and M246, P248, and V249 of IL3Rα were the most promising residues to target. T348W of βc showed a reduction of maximal cell proliferation response among the single βc mutants generated (Supplementary Fig. S3A). Double and triple mutations of IL3Rα residues 246, 248, and 249 also showed a significant reduction (60%) of maximal cell proliferation (Supplementary Fig. S3B), with mutations of P248 to bulky side chains (L, K, F, and W) alone all showing a reduction in proliferation similar to the double and triple mutants (Supplementary Fig. S3C). This proline residue resides in a loop that is close to the βc interface and its mutation to larger residues is predicted to introduce more flexibility into the loop and cause steric clashes. After establishing that IL3Rα P248 is important for IL3 function (Supplementary Fig. S3B and S3C), we then confirmed that expression of the IL3Rα P248L mutant did not adversely affect cell-surface IL3Rα through multiple independent assays: cell-surface expression through flow cytometry (Supplementary Fig. S3D), low- and high-affinity binding of IL3 through radioligand binding assays (Supplementary Fig. S3E), and IL3Rα stability at the cell surface through tracking of biotinylated IL3Rα (Supplementary Fig. S3F). Collectively, these

Figure 2. The IL3R heterodimer forms hexameric complexes that assemble into dodecamers in solution and at the cell surface. **A,** Surface view of the IL3R hexamer dimerizing into an IL3R dodecamer through a unique "assembly interface" indicated by the light gray box. Components are colored using light and dark shades to distinguish the two hexamers. **B,** Cartoon of the IL3R hexamer complex (side view) showing the βc homodimer (shades of blue) in the center, with IL3–IL3Rα binary complexes (orange and pink) binding symmetrically to each end. The hexamer assembles through interfaces at sites 1 to 3. The IL3Rα N-terminal domain (NTD) and domains D2 and D3 are indicated, as are βc domains D1 to D4. **C,** Details of the side chain interactions in half of the "assembly interface" that dimerizes two IL3R hexamers (view looking up from the membrane surface). The second half of the "assembly interface" occurs between the same residues but is located in IL3Rα D3 and βc' D4 (Supplementary Fig. S2E). Details of sites 1 to 3 and the "assembly interface" interactions are summarized in Supplementary Table S2. Polar bonds are depicted as black dashed lines. **D,** Left: schematic of IL3Rα–IL3Rα' and IL3Rα–βc fluorescence lifetime imaging-FRET experiments. For IL3Rα–IL3Rα' FRET experiments ($n = 4$), wild-type IL3Rα fused to cytoplasmic SYFP2 (indicated as V) or mScarlet-I (indicated as S) and truncated βc homodimer were expressed in cells. For IL3Rα–βc FRET experiments ($n = 3$), wild-type IL3Rα fused to cytoplasmic mScarlet-I (indicated as S) and truncated βc homodimer fused to cytoplasmic SYFP2 (indicated as V) were expressed in cells. Right: %FRET efficiencies were derived from fluorescence lifetimes of SYFP2 donor ± IL3 across cells. **E,** Same as for **D** but using P248L IL3Rα [IL3Rα–IL3Rα' experiments ($n = 4$) and IL3Rα–βc experiments ($n = 3$)].

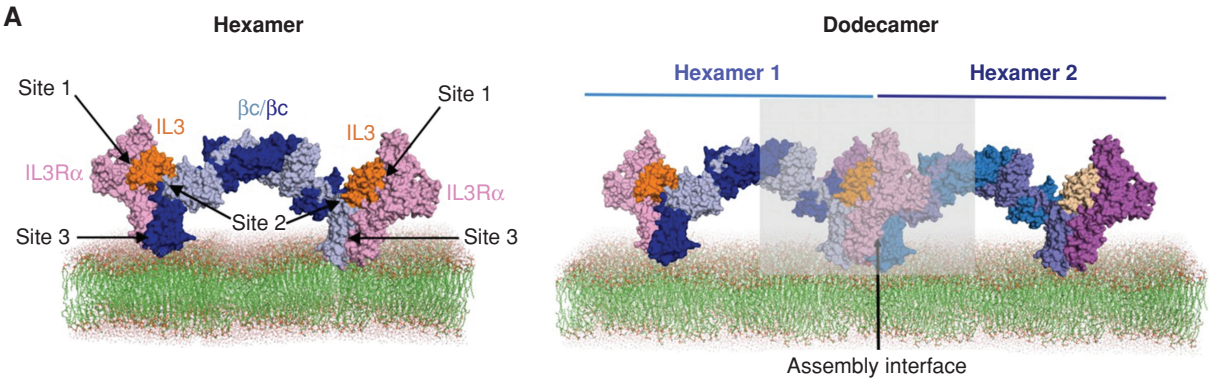

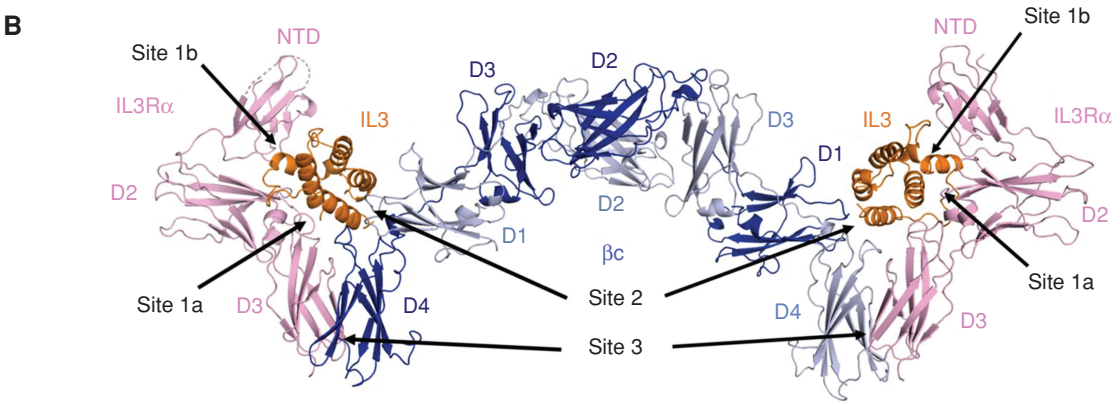

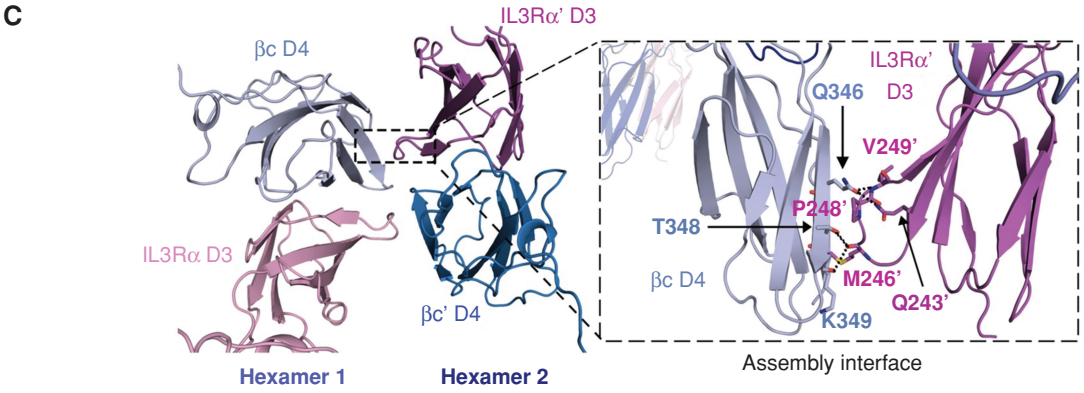

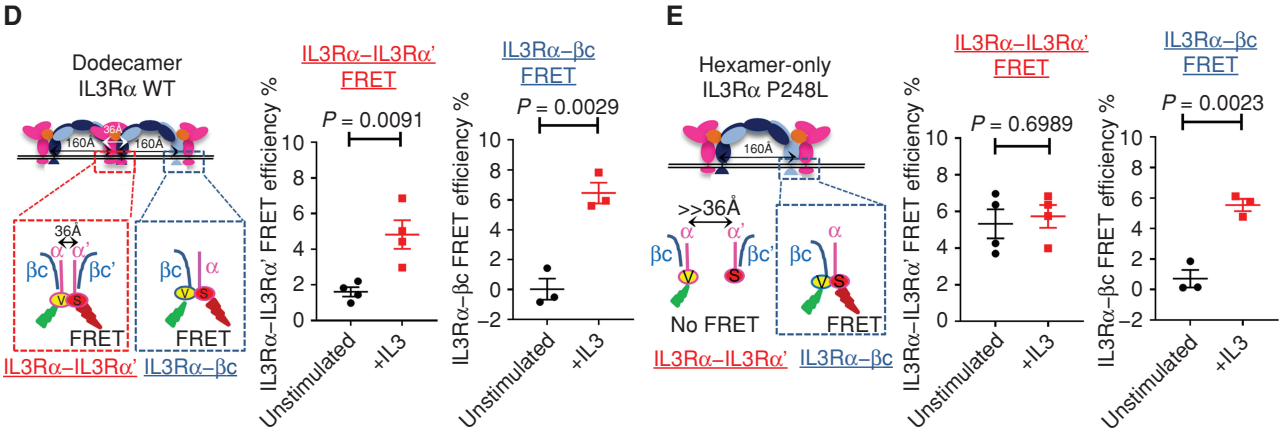

analyses were consistent with the formation of an IL3R hexamer. Because the distance between the C-terminal ends of IL3Rα subunits ranges from ~160 Å in the hexamer complex to ~36 Å in the dodecamer complex, we were able to use fluorescence resonance energy transfer (FRET) imaging (42–44) between fluorescently tagged IL3Rα subunits to assess the formation of higher-order IL3R complexes on the cell surface (Fig. 2D and E). SYFP2 (donor) and mScarlet-I (acceptor) fluorescent proteins were fused as FRET pairs to the C-terminal end of wild-type (WT) IL3Rα subunits. FRET was then measured in the presence of untagged βc at the plasma membrane using donor (SYFP2) fluorescence lifetime imaging (FLIM). IL3 caused a 3.2% ± 0.5% increase in IL3Rα–IL3Rα' FRET efficiency (Fig. 2D; Supplementary Fig. S3G), confirming the formation of a higher-order IL3R complex at the cell surface. In contrast, there was no change in IL3Rα–IL3Rα' FRET efficiency in cells coexpressing IL3Rα P248L–SYFP2 and P248L–mScarlet-I (Fig. 2E; Supplementary Fig. S3H), indicating that IL3Rα P248L did not form higher-order receptor complexes. Importantly, IL3Rα P248L retained the ability to associate with βc, as shown by fusing SYFP2 to βc and coexpressing βc–SYFP2 with IL3Rα–mScarlet-I or IL3Rα P248L–mScarlet-I (Fig. 2D and E; Supplementary Fig. S3I). Therefore, IL3Rα P248L can form hexameric IL3R complexes but is selectively deficient at forming higher-order IL3R assemblies, providing a platform to examine the signaling consequences arising from variations in receptor oligomerization.

The Hexameric and Dodecameric Forms of IL3R Bias Signaling, Segregating Stemness versus Differentiation Programs

To examine whether altered receptor assemblies can affect biology directly, we first used murine fetal liver-derived hematopoietic (FDH) cells from $\beta c^{-/-}$ and $\beta_{IL3}^{-/-}$ mice immortalized through doxycycline-inducible HoxA9 expression (45–47) and stably expressing human βc and either IL3Rα WT or P248L. Following IL3 stimulation, the P248L-transduced cells (IL3R hexamer) gave rise to myeloid blasts consistent with a primitive phenotype and in contrast to FDH cells in which IL3Rα WT (IL3R dodecamer) induced monocytic cell differentiation (Fig. 3A and B). Overall, FDH cells expressing the IL3R hexamer showed (i) a reduced proportion of $CD11b^+Gr1^+$ cells (Fig. 3C), (ii) reduced cell-surface expression of mature lineage markers (Fig. 3D), and (iii) reduced expression of monocytic genes (Supplementary Fig. S3J). Furthermore, we detected increased cell-surface expression of CD117, a marker expressed in primitive hematopoietic stem and progenitor cells (HSPC; Fig. 3E). There was also increased expression of genes associated with HSPCs (48) in cells expressing the IL3R hexamer compared with cells expressing the IL3R dodecamer (Fig. 3F). Expression of the IL3R hexamer induced a quiescent, stem-like phenotype with an increased proportion of cells arrested in G_0 (Fig. 3G) and increased cell survival (Fig. 3H). In long-term cultures, cells expressing the IL3R hexamer showed sustained growth and expansion, while cell counts for cultures expressing the IL3R dodecamer started to decline (Supplementary Fig. S3K). FDH cell lines expressing other IL3Rα P248 mutants also showed similar impaired differentiation (Supplementary Fig. S3L and S3M) and increased expression of CD117 (Supplementary Fig. S3N).

In an independent model using primary murine HSPCs (49), we also found that cells expressing βc and IL3Rα P248L had higher cell survival (Supplementary Fig. S3O) and a more immature stem-like phenotype with a higher frequency of Lin^-CD117^+ cells (Fig. 3I) that ultimately gave rise to a higher number of clonogenic cells (Fig. 3J). Importantly, in serial replating experiments (Fig. 3K), cells expressing βc and IL3Rα P248L showed a mild extension of colony numbers to a fourth plating. By contrast, cells expressing βc and IL3Rα WT lost their replating potential after the fourth round of plating (Fig. 3K), and there was no difference between IL3Rα P248L and WT when stimulated with a cytokine cocktail (Supplementary Fig. S3P). The data suggest that biasing IL3R assembly toward its hexameric form (IL3Rα P248L) confers a more primitive stem-like phenotype, whereas its dodecameric form (IL3Rα WT) induces monocytic differentiation.

To understand the receptor proximal signaling underpinning the dichotomy of stemness versus differentiation mediated by the two IL3R assemblies, we performed a reverse phase protein array (RPPA) screen that revealed quantitative and qualitative differential signaling profiles for FDH cells expressing IL3R hexamer versus dodecamer (Supplementary Fig. S4A). Cells expressing P248L IL3R showed greatly reduced induction of tyrosine phosphorylation of STAT1 upon IL3 stimulation, with no differences in phosphorylation of STAT5, which was further confirmed by immunoblotting (Fig. 4A). As STAT1 has been previously shown to be important for differentiation (50, 51), we performed knockdown of STAT1 in FDH cells expressing βc and IL3Rα WT (Supplementary Fig. S4B) to determine the functional relevance of STAT1 signaling in the differentiation process. Expression of two independent STAT1 short hairpin RNAs (shRNA) resulted in marked inhibition of differentiation, as demonstrated by a lower abundance of $CD11b^+Gr1^+$ cells (Fig. 4B)

Figure 3. The IL3R hexamer induces a stemness phenotype. **A** and **B,** Morphology of FDH cells expressing βc and IL3Rα P248L (hexamer) or WT (dodecamer) cultured with SCF or IL3 for 5 days, as assessed by May–Grunwald and Giemsa staining. Scale bars, 100 μm. Images from a representative experiment are shown, with quantification of cell types shown for 3 independent experiments in **B**. **B,** FDH cells cultured with IL3 were characterized as granulocyte-like (blue), monocyte/macrophage-like (orange), or myeloid blasts (green) and quantified after IL3 treatment for 5 days ($n = 3$). **C,** Representative flow cytometric plot (left) for determination of the $\%CD11b^+Gr1^+$ population in FDH cells expressing βc and IL3Rα P248L or WT and quantification of $\%CD11b^+Gr1^+$ cells (right, $n = 6$). **D,** Representative flow cytometric histograms (left) for determination of ΔMFI for expression of mouse lineage cocktail in FDH cells expressing βc and IL3Rα P248L or WT (right, $n = 3$). Gray: isotype control; red: lineage antibody cocktail. ΔMFI: stained minus isotype control median fluorescence intensity. **E,** Same as for **D**, but for CD117 expression in FDH cells expressing βc and IL3Rα P248L or WT ($n = 4$). **F,** Expression of genes associated with stem and progenitor cells in FDH cells expressing βc and IL3Rα P248L or WT after IL3 treatment for 2 days normalized to RPLP0 expression. **G,** Quiescent FDH cells as assessed by % $BrdUrd^-$ cells arrested in G_0 using BrdUrd and 7-AAD flow cytometric analysis after IL3 treatment for 2 days ($n = 3$). **H,** FDH cell survival measured by Annexin V (Ann V)–negative staining following IL3 withdrawal ($n = 3$). **I** and **J,** Fetal liver cells from $\beta c^{-/-}\beta_{IL3}^{-/-}$ mice were transduced to express βc and IL3Rα P248L (blue) or WT (red) and assessed for the $\%Lin^-CD117^+$ population (**I**) after 10 days of IL3 treatment ($n = 4$) and subsequent colony formation (**J**; $n = 3$). **K,** Time course of serial replating colony counts of $\beta c^{-/-}\beta_{IL3}^{-/-}$ mouse fetal liver cells expressing βc and IL3Rα P248L (blue) or WT (red) and cultured in IL3 alone ($n = 3$).

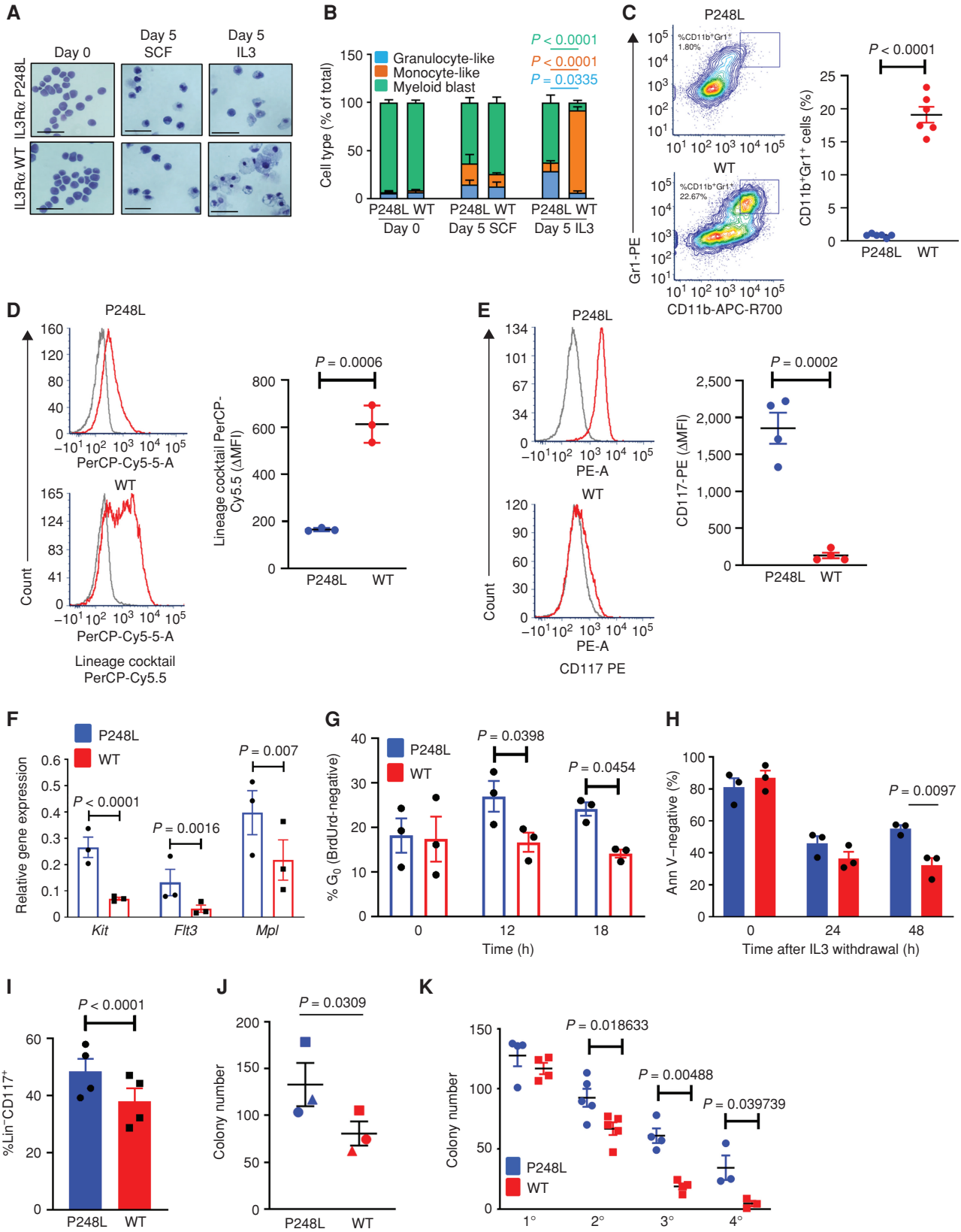

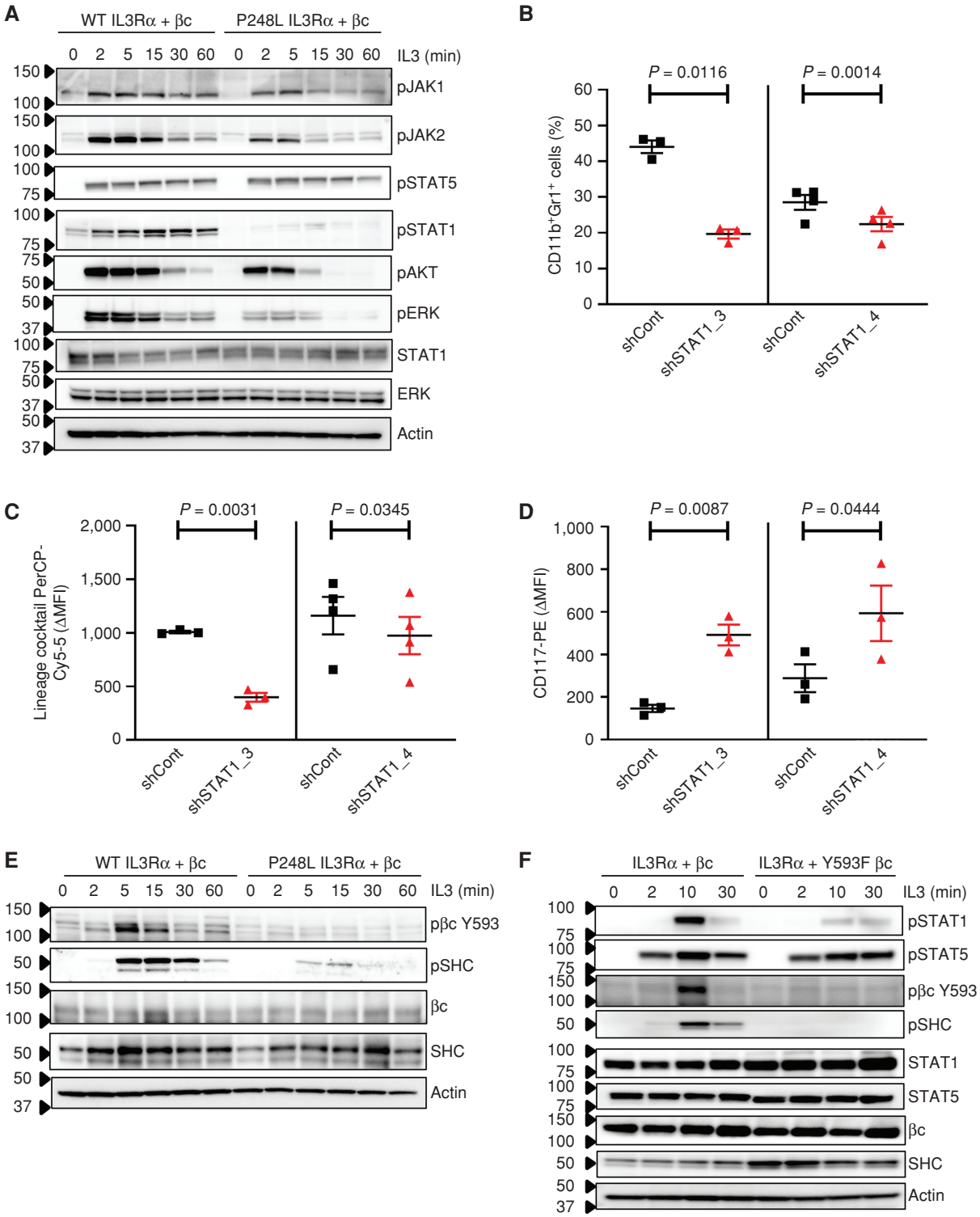

Figure 4. The IL3R hexamer biases STAT signaling toward stemness. **A,** Time course of IL3 stimulation of FDH cells expressing βc and IL3Rα WT (dodecamer) or P248L (hexamer). Cell lysates were immunoblotted with antibodies against indicated phosphorylated and total proteins. **B,** Flow cytometric analysis of %CD11b$^+$Gr1$^+$ in FDH cells expressing βc and IL3Rα WT transduced with lentivirus encoding control (shCont, black) or STAT1 (shSTAT1_3 or shSTAT1_4, red) shRNA after treatment with IL3 for 2 days ($n = 3$). **C,** Flow cytometric analysis of mouse lineage cocktail expression by ΔMFI (stained minus unstained median fluorescence intensity) in FDH cells expressing βc and IL3Rα WT transduced with shCont, shSTAT1_3, or shSTAT1_4 ($n = 3$). **D,** Flow cytometric analysis of CD117 expression in cells as for **C** after IL3 treatment for 2 days ($n = 3$). ΔMFI as for **C**. **E,** Time course of IL3 stimulation of FDH cells expressing βc and IL3Rα WT or P248L. Cell lysates were immunoblotted with antibodies against indicated phosphorylated and total proteins. **F,** Time course of FDH cells expressing IL3Rα and βc WT or βc Y593F and stimulated with IL3 for up to 30 minutes. Cell lysates were immunoblotted with antibodies against indicated phosphorylated and total proteins. For **A**, **E**, and **F,** representative immunoblots are shown from 3 independent experiments.

and a lower expression of mature lineage markers (Fig. 4C). Conversely, expression of cell-surface CD117 (Fig. 4D) as well as expression of genes commonly associated with stemness (Supplementary Fig. S4C) and cell survival (Supplementary Fig. S4D) were increased upon shSTAT1, partially recapitulating the IL3R hexamer phenotype (Fig. 3C–F and H). These findings implicate STAT1 as a downstream effector of dodecamer signaling regulating the transition from stemness to differentiation.

As Y593 in βc regulates HSPC differentiation and proliferation (49) and is part of a SHC-binding motif and predicted to be a docking site for STAT1, we next examined its role in uncoupling STAT1 from the IL3R hexamer. In contrast to IL3Rα WT, the IL3Rα P248L did not phosphorylate βc Y593 or SHC itself (Fig. 4E), and mutation of βc at Y593 precluded tyrosine phosphorylation of STAT1, but not of STAT5 (Fig. 4F). Thus, these data provide a causal link between βc Y593 phosphorylation and activation of STAT1 and a mechanistic explanation for the hexamer-induced bias toward a stemness phenotype.

The Hexameric IL3R Induces an HSPC-like Transcriptional State

To gain insight into the transcriptional programs of FDH cells expressing either the IL3R hexamer or dodecamer after IL3 stimulation, RNA sequencing (RNA-seq) was undertaken, followed by GSEA (Fig. 5A and B; Supplementary Fig. S4E). The hexamer program was enriched for gene sets associated with HSPC maintenance (Fig. 5C and D), stemness, and self-renewal (34), including the unfolded protein response (Supplementary Fig. S4F; ref. 52). Conversely, gene sets characteristic for myeloid differentiation (ref. 53; Fig. 5E and F) and eosinophil activation (54) showed negative enrichment (Supplementary Fig. S4G). Furthermore, the hexamer failed to induce IFNα and IFNγ-response genes (Supplementary Fig. S4H and S4I) and demonstrated negative enrichment for genes commonly upregulated by STAT1 (ref. 55; Supplementary Fig. S4J), which is analogous to an IFN-refractory stem-like state (56) and consistent with reduced STAT1 phosphorylation (Fig. 4A).

To determine if the hexamer- versus dodecamer-induced signaling and stemness programs uncovered from cell model studies were relevant to primary human AML samples, we began by deriving a hexamer versus dodecamer signature from the FDH model and performing gene set variability analysis (GSVA) across multiple patient cohorts (25, 26, 57). Hexamer signaling was highly enriched in the most primitive M0 French–American–British classification (FAB) subtype (Fig. 6A; Supplementary Fig. S5A) and in *FLT3*-ITD– and *RUNX1*-mutated, high IL3Rα/βc ratio (Supplementary Fig. S1F) AML subtypes (Fig. 6B; Supplementary Fig. S5B and S5C; ref. 58). Genes downregulated in AML samples with a high IL3Rα/βc ratio were also negatively enriched in IL3R hexamer expressing FDH cells (Fig. 6C). In accordance, hexamer signature scores of 10 primary AML samples (Fig. 1D) were significantly higher in the high IL3Rα/βc transcript ratio samples (Fig. 6D) and correlated positively with the relative abundance of the IL3Rα^{hi}βc^{lo} fraction (Supplementary Fig. S5D).

To focus on the transcriptional programs linked to both the IL3Rα/βc ratio and IL3-induced hexamer versus dodecamer signaling directly relevant to AML, we integrated the genes from the initial signature (Fig. 5) with the genes that are positively or negatively correlated with the IL3Rα/βc cell-surface protein ratio in primary AML patient samples. This provided a new "intersect" hexamer and dodecamer signature (Fig. 6E; Supplementary Fig. S5E). By GSVA, this intersect hexamer versus dodecamer signature scored highest in (i) patient samples classified with our recently developed hierarchy-classification method as primitive versus mature (ref. 32; Fig. 6F; Supplementary Fig. S5F); (ii) the primitive CD34$^+$ fractions versus CD34$^-$ fractions (refs. 20, 32; Fig. 6G; Supplementary Fig. S5G and S5H); (iii) stem and progenitor cell types from an independent AML patient dataset (ref. 35; Fig. 6H); (iv) the primitive HSPC fractions of normal human CB (refs. 36, 37; Fig. 6I; Supplementary Fig. S5I) and bone marrow controls (ref. 35; Supplementary Fig. S5J); and (v) LSC$^+$ engrafting versus nonengrafting (LSC$^-$) fractions across our AML RNA-seq (ref. 32; Fig. 6J) and microarray (20) datasets (Supplementary Fig. S5K). Notably, the highest scores among LSC$^+$ fractions were detected in those with the highest frequency of functionally defined LSCs (refs. 20, 39; Fig. 6K; Supplementary Fig. S5L), directly linking the hexamer response to LSC potential. Collectively, these data strongly support the concept that stemness in cellular hierarchies is promoted by hexamer assembly that derives from the elevated IL3Rα/βc ratio found on primitive cells.

Higher IL3Rα/βc Ratios Bias toward IL3R Hexameric Assembly and Maintain a Primitive Leukemic Cell Phenotype *In Vivo*

To provide direct evidence that an elevated IL3Rα/βc ratio biases the formation of hexamers, we modulated the IL3Rα versus βc ratio on the cell surface and undertook three analytical approaches: (i) monitoring of receptor assembly, (ii) analysis of biased STAT signaling, and (iii) assessing the functional consequences on stemness and differentiation in AML. Receptor assembly was investigated using "gold standard" FLIM-FRET analysis in HEK293T cells in which coexpression of βc–SYFP2 and βc–mScarlet-I at equimolar levels (59) with IL3Rα–mCerulean allowed us to analyze FLIM-FRET between βc–βc' subunits that occur at the assembly interface for dodecamer formation, together with precise and simultaneous quantification of the IL3Rα and βc expression ratio on the cell surface in fluorescence units (Fig. 7A), enabling us to directly link IL3Rα/βc ratios to hexamer or dodecamer assembly. First, we found that IL3 induced a comparable increase in FRET between IL3Rα and βc in cells coexpressing IL3Rα–mScarlet-I, βc–SYFP2, and βc–mCerulean regardless of whether they had a high or low IL3Rα/βc ratio (Fig. 7B; Supplementary Fig. S6A and S6B), consistent with hexamer assembly (Fig. 2D and E). Next, we observed that cells with lower IL3Rα/βc ratio showed a significant increase in βc–βc' FRET efficiency after IL3 stimulation (Fig. 7C; Supplementary Fig. S6C and S6D), consistent with dodecamer assembly (Fig. 2D). Importantly, at higher IL3Rα/βc ratio, βc–βc' FRET was absent (Fig. 7C), providing direct evidence that higher IL3Rα/βc ratios on the cell surface bias toward a predominantly hexameric assembly, whereas lower ratios bias toward a dodecameric assembly.

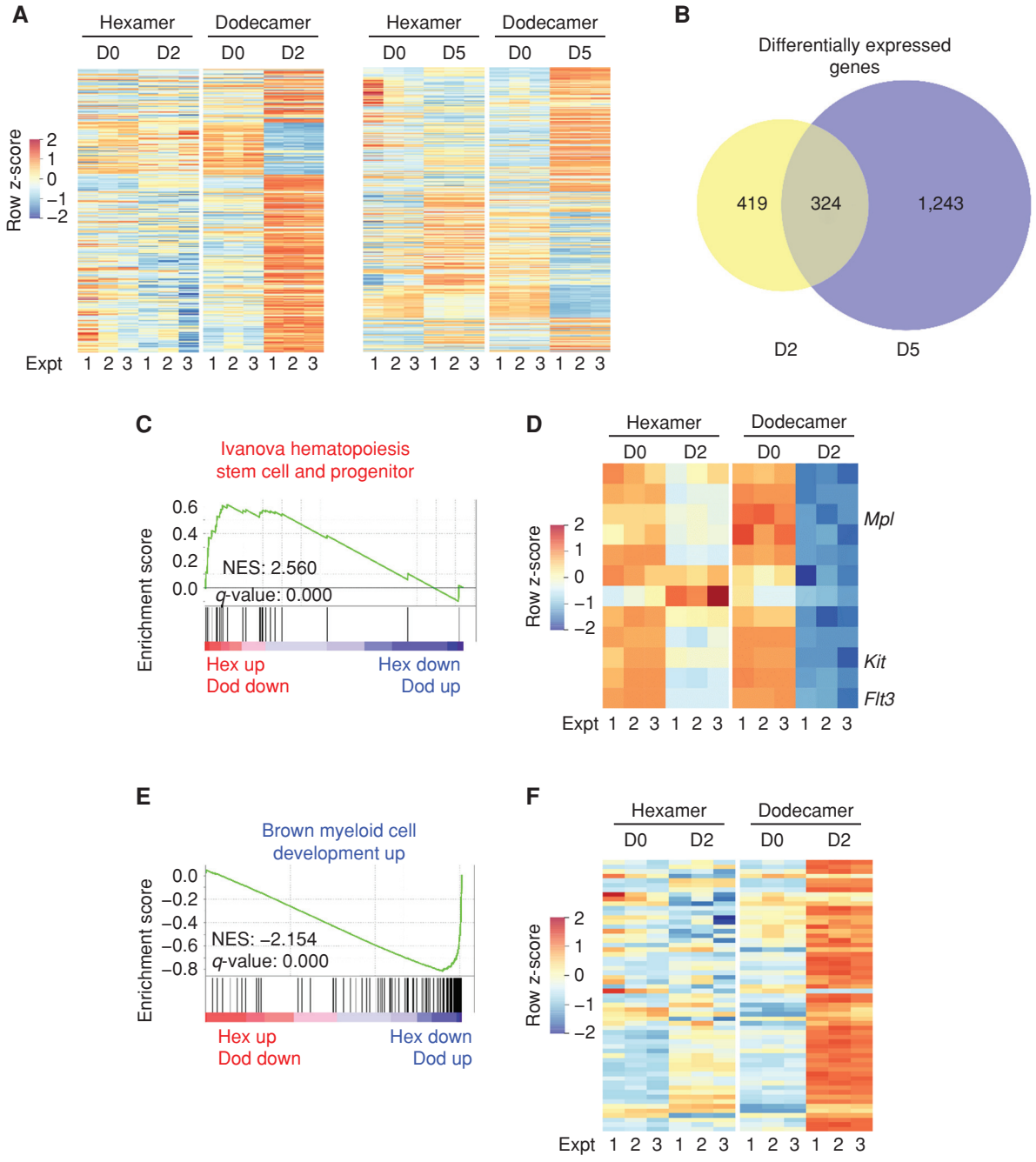

Figure 5. The hexameric IL3R induces an HSPC-like transcriptional state. **A,** Heat map showing differential gene expression data in FDH cells expressing βc and IL3Rα P248L (hexamer) or WT (dodecamer) after 2 and 5 days of IL3 treatment for 3 independent experiments (Expt). **B,** Number of differentially expressed genes between cells expressing hexameric versus dodecameric IL3R after 2 and 5 days of IL3 treatment. q < 0.05, fold change >2. **C,** GSEA plot showing enrichment of the stem/progenitor cell signature in FDH cells expressing βc and IL3Rα P248L. Dod, dodecameric; Hex, hexameric; NES, normalized enrichment score. **D,** Heat map showing enrichment of the stem/progenitor cell signature in FDH cells expressing βc and IL3Rα P248L with specific genes. **E,** GSEA plot showing loss of the myeloid cell differentiation signature in cells expressing the IL3R hexamer. **F,** Heat map showing negative enrichment of the myeloid cell differentiation signature in cells expressing βc and IL3Rα P248L.

To investigate STAT1 signaling, we used the FDH cell system expressing βc and IL3Rα WT and analyzed the levels of phosphorylated STAT1 and STAT5 after IL3 stimulation with varying IL3Rα and βc surface levels using flow cytometry. At constant βc levels, FDH cells with the top 15% IL3Rα expression had reduced STAT1 phosphorylation compared with cells with the bottom 15% IL3Rα expression (Supplementary Fig. S6E). Conversely, at constant IL3Rα levels, FDH cells with high βc expression exhibit increased STAT1 signaling compared with cells with low βc expression (Supplementary Fig. S6E). As controls, levels of phosphorylated STAT5 were essentially unaltered regardless of changes in

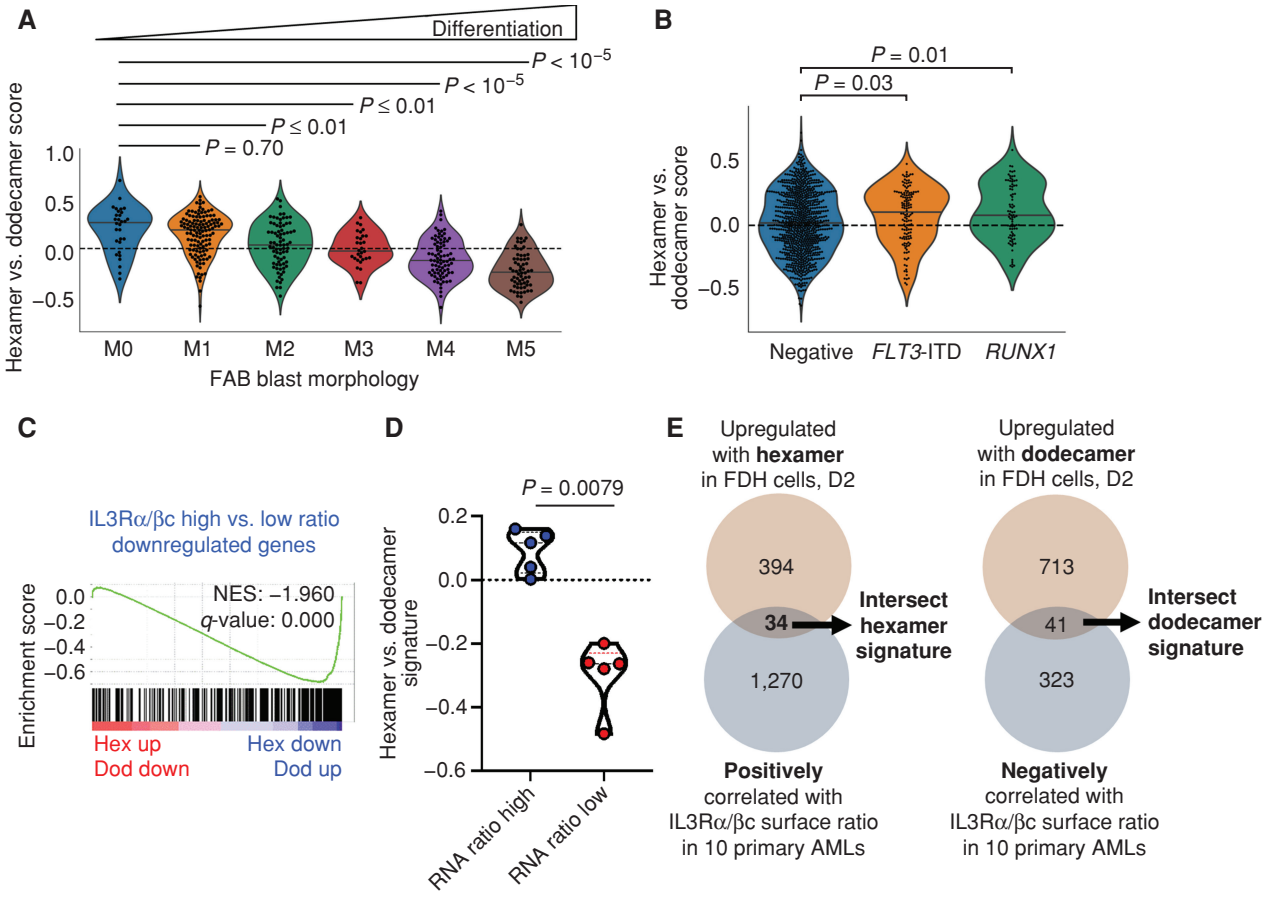

Figure 6. Higher IL3Rα/βc ratios bias hexamer signaling to promote leukemia stemness programs. **A,** GSVA showing hexamer versus dodecamer signature enrichment in AML FAB subtypes [The Cancer Genome Atlas (TCGA), Beat AML, and Leucegene; refs. 25, 26, 57]. **B,** GSVA plot showing enrichment of the hexamer vs. dodecamer signature in *FLT3*-ITD– and *RUNX1*-mutant AML patients (Beat AML and TCGA; refs. 25, 26). Dod, dodecameric; Hex, hexameric; NES, normalized enrichment score. **C,** GSEA plot showing downregulated genes from IL3Rα/βc-high transcript ratio AML patient samples are enriched in the downregulated genes in the hexamer gene signature. **D,** Hexamer vs. dodecamer signature GSVA scores in the immunophenotypically characterized primary AML patient samples with high (indicated in blue) and low (indicated in red) IL3Rα/βc transcript ratio (Toronto cohort). **E,** Schematic for generation of the intersect hexamer and dodecamer gene signatures linking IL3Rα/βc cell-surface protein ratio and hexamer vs. dodecamer signaling. (*continued on next page*)

IL3Rα or βc levels (Supplementary Fig. S6F), in accordance with our data on FDH cells expressing P248L IL3R (Fig. 4A; Supplementary Fig. S4A).

Finally, to investigate the functional impact of biasing IL3R stoichiometry on the human AML hierarchy, we used lentivectors expressing IL3Rα P248L or overexpressing IL3Rα WT to increase the IL3Rα/βc ratio and enforce hexamer signaling in a novel primary AML patient-derived model we recently developed (OCI-AML22; ref. 60). OCI-AML22 is unique in that it recapitulates the functional and transcriptomic cellular hierarchy of primary samples, with functional LSC highly enriched in the $CD34^+CD38^-$ compartment (60). Consistent with our data on primary AML, the highest IL3Rα/βc transcript (Supplementary Fig. S6G and S6H), cell-surface protein expression ratios (Fig. 7D; Supplementary Fig. S6I), and hexamer signature scores (Fig. 7E) were seen in the functional LSC-enriched and IL3-dependent $CD34^+CD38^-$ fraction (Supplementary Fig. S6J). Furthermore, IL3 stimulation induced the highest pSTAT5 response in the IL3Rα/βc ratio–high $CD34^+$ fractions without concomitantly inducing STAT1 phosphorylation (Supplementary Fig. S6K), recapitulating the signaling results from our FDH model (Fig. 4) and further confirming the validity of the OCI-AML22 model to investigate the functional effects of altering IL3R stoichiometry in a human AML cell context. Inspired by our functional data from FDH cells (Fig. 3G) and the quiescence signature found in high IL3Rα/βc ratio AML samples (Fig. 1D, F, and G), we performed cell-cycle analysis of lentivector transduced (BFP^+) and LSC-enriched ($CD34^+CD38^-$) OCI-AML22 cells. Compared with control, IL3Rα P248L induced a greater restraint of cells in the canonical G_0 ($Ki\text{-}67^-$) phase (Fig. 7F) and in a deeply dormant, CDK6-negative state (refs. 38, 61; Fig. 7G). Consistent with increased quiescence in the LSC-enriched fraction, OCI-AML22 cells overexpressing IL3Rα P248L showed a lower proportion of $CD34^+CD38^-$ cells (Fig. 7H). These findings were also recapitulated in another hierarchical AML cell model (OCI-AML8227; refs. 38, 62; Supplementary Fig. S6L–S6O). To confirm that quiescence induction and reduced generation of $CD34^+CD38^-$ cells are not compromising engraftment potential, and to assess the

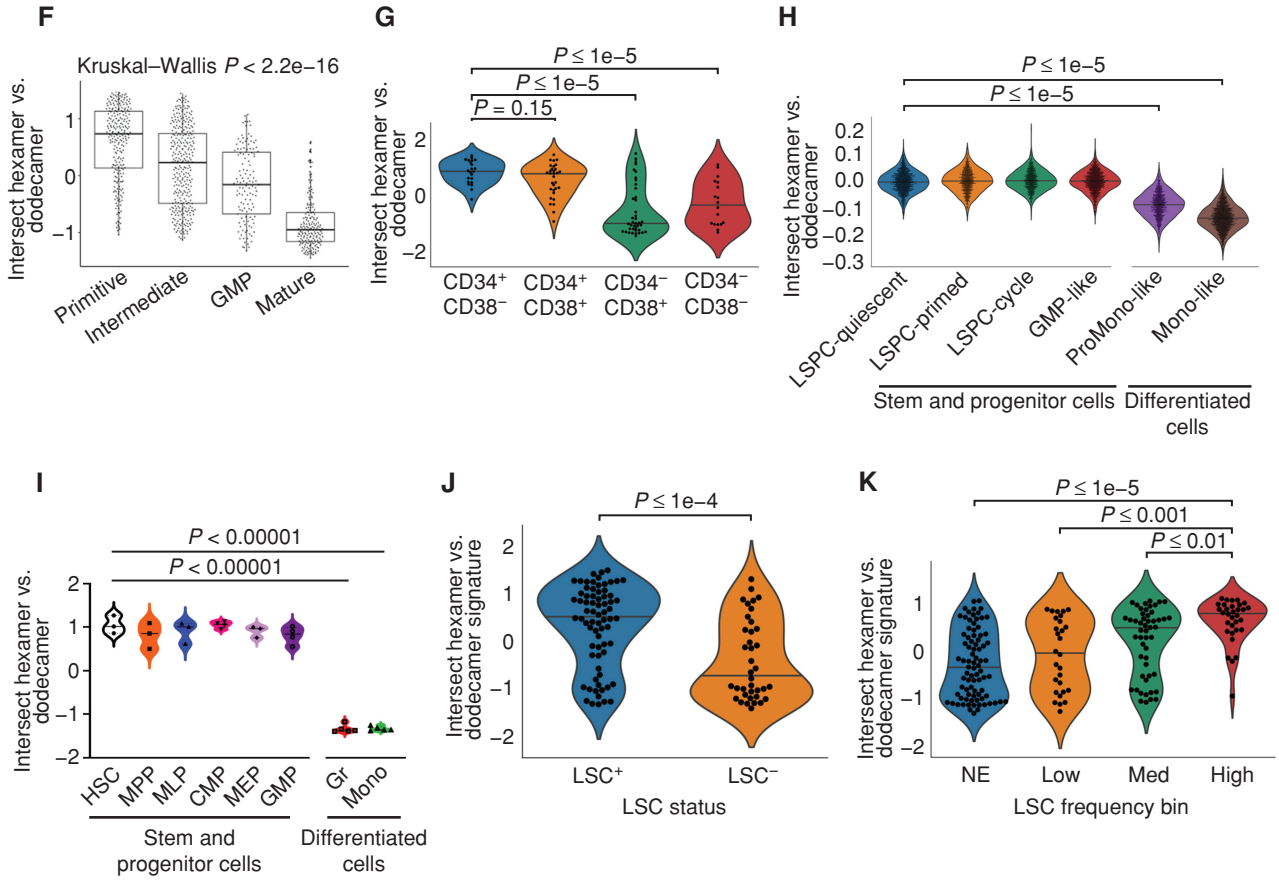

Figure 6. ***(Continued)*** **F,** GSVA demonstrating the enrichment of the intersect hexamer vs. dodecamer signature in AML patient samples with primitive cellular hierarchy (32). **G,** GSVA plot showing enrichment of the intersect hexamer vs. dodecamer signature in more primitive fractions (as defined by CD34 CD38 expression) from primary AML patient samples ($n = 110$ RNA-seq; ref. 32). **H,** GSVA plot showing enrichment of the intersect hexamer vs. dodecamer signature in stem and progenitor cells in the leukemia cellular hierarchy (32, 35). **I,** Enrichment of the intersect hexamer vs. dodecamer signature in more primitive sorted populations from CB (36, 37). CMP, common myeloid progenitors; GMP, granulocyte-monocyte progenitors; Gr, granulocytes; HSC, hematopoietic stem cells; MEP, megakaryocyte-erythroid progenitors; MLP, multilymphoid progenitors; Mono, monocytes; MPP, multipotent progenitors. **J,** The intersect hexamer vs. dodecamer signature (GSVA) is enhanced in LSC$^+$ (engrafting) over LSC$^-$ (nonengrafting) fractions (32). **K,** Enrichment of the intersect hexamer vs. dodecamer signature in patients with higher LSC frequency compared with nonengrafting (NE) fractions (20).

effects of overexpression of IL3Rα WT and IL3Rα P248L on differentiation in AML, we transplanted transduced CD34$^+$ OCI-AML22 cells into NSG-SGM3 mice expressing human IL3 (Fig. 7I). At 12 weeks, there was no evidence that the repopulation capacity of engrafting LSC was impaired: The total (% human CD45$^+$) or relative (% BFP$^+$; compared with input BFP levels) engraftment potential for either group with IL3Rα WT and IL3Rα P248L (hexamer) groups (and showing higher IL3Rα/βc ratios vs. control) was similar to control engrafted mice (Supplementary Fig. S7A–S7C). Consistent with the *in vitro* data, expression of IL3Rα P248L and IL3Rα WT resulted in a reduced proportion of BFP$^+$CD34$^+$CD38$^-$ cells *in vivo* (Fig. 7J; Supplementary Fig. S7D). We further observed a concomitant suppression of differentiation into a mature granulocyte-like (SSC^{hi}, CD66$^+$) population in both hexamer assembly-promoting groups compared with control (Fig. 7K; Supplementary Fig. S7E). Furthermore, analysis of 156 previously reported xenografts that we had generated from 33 RNA-seq profiled AML patient samples (63) showed that the intersect hexamer versus dodecamer signature positively correlated with the percentage of undifferentiated cells (%CD15$^-$CD14$^-$, $P = 0.015$) and negatively with %CD15$^+$ ($P = 0.043$) and %CD14$^+$ cells ($P = 0.021$) within the AML grafts (Supplementary Fig. S7F). Among these xenografted primary samples are seven of the 10 transcriptionally and immunophenotypically profiled samples (Toronto cohort; Figs. 1D and 6D). The high-ratio samples generated significantly more undifferentiated (%CD15$^-$CD14$^-$) and less differentiated (%CD15$^+$) output *in vivo* than the low-ratio samples (Fig. 7L). Similarly, from the two AML samples (#140005 and #130578) that we fractionated for high-, med-, and low-surface IL3Rα/βc ratio and transplanted into NSG and NSG-SGM3 mice (Fig. 1J and K), the xenografts transplanted with the higher-ratio fractions also generated more undifferentiated (%CD34$^+$CD14$^-$) and less differentiated output (%CD14$^+$) compared with lower-ratio fractions (Supplementary Fig. S7G). Consistent with the *in vitro* functional data across several cell models and the detailed transcriptional analysis on primary AML, these *in vivo* data functionally establish that higher IL3Rα/βc ratios and the IL3R hexamer stoichiometry drive stemness and block differentiation in AML.

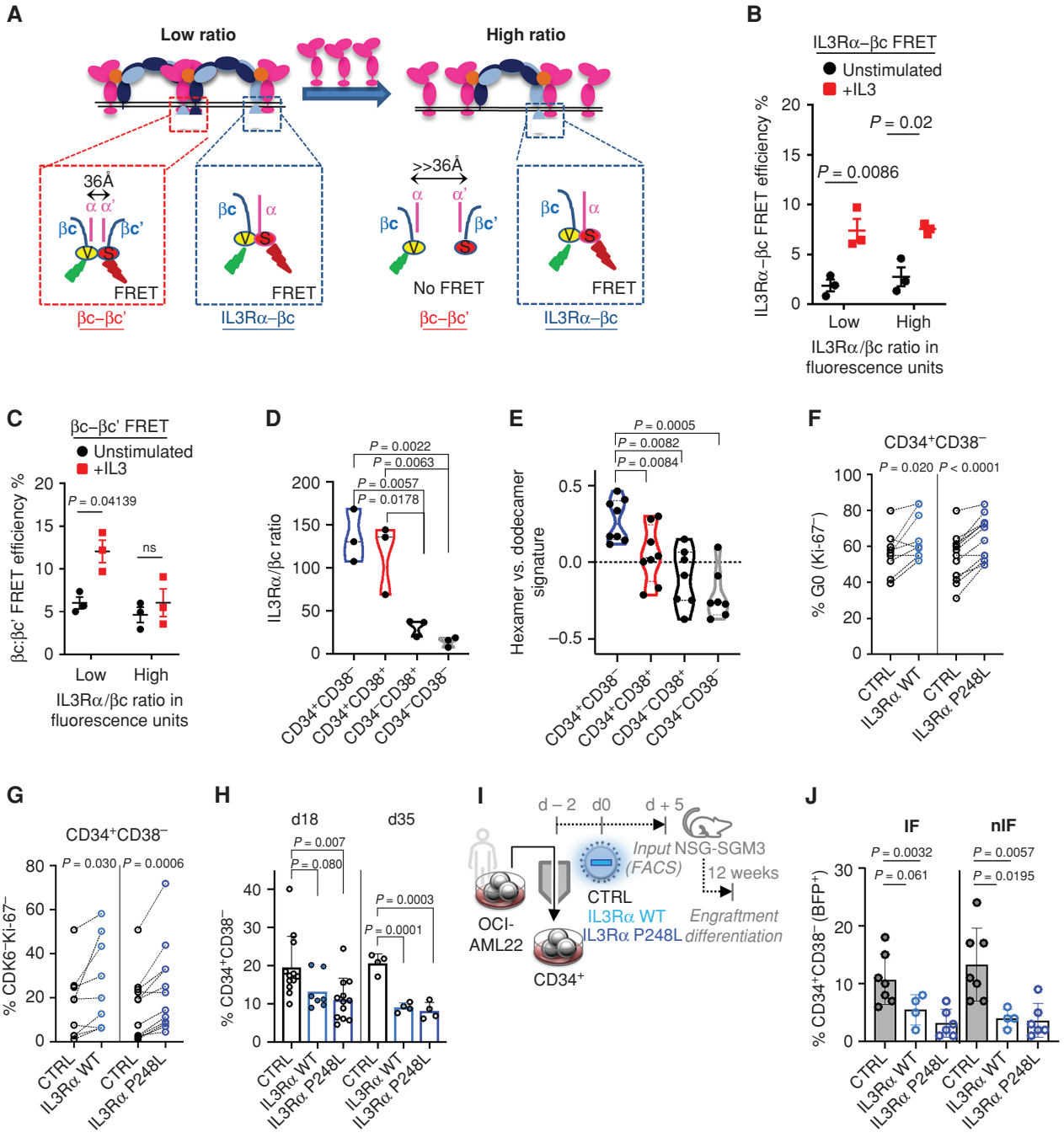

Figure 7. Higher IL3Rα/βc ratios induce hexameric receptor assembly at the cell surface and maintain the leukemic primitive cell phenotype *in vivo*. **A,** Schematic of IL3Rα–βc ($n = 3$) and βc–βc' ($n = 3$) FLIM-FRET experiments using truncated βc fusion proteins with SYFP2 (V) or mCerulean and IL3Rα fusion proteins with mScarlet-I (S) for IL3Rα–βc FRET and truncated βc fusion proteins with SYFP2 (V) and mScarlet-I (S) and IL3Rα fusion proteins with mCerulean for βc–βc' FRET. **B** and **C,** %IL3Rα–βc (**B**) and %βc–βc' (**C**) FRET efficiencies were derived from fluorescence lifetimes of βc-SYFP2 donor unstimulated (indicated by black dots) and IL3 treatment (indicated by red squares) across cells with high and low expression of IL3Rα/βc ratio in fluorescence units. ns, not significant. **D,** Cell-surface IL3Rα/βc protein expression ratio in CD34 and CD38 defined subpopulations of OCI-AML22 ($n = 3$ independent cultures). **E,** Hexamer vs. dodecamer signature scores (GSVA) in the indicated sorted subpopulations of the primary AML patient-derived LSC model OCI-AML22 (RNA-seq, $n = 8$ freshly thawed and various culture time points combined). **F** and **G,** Intracellular Ki-67 (**F**) and CDK6 (**G**) staining of sorted BFP+CD34+CD38− OCI-AML22 cells 4 weeks after transduction with IL3Rα WT or P248L (IL3R hex; $n = 7$ individual culture passages and transductions, 2 independent experiments). **H,** Quantification of the BFP+CD34+CD38− population in OCI-AML22 cells 18 and 35 days after transduction with control vector, IL3Rα WT, or IL3Rα P248L ($n = 7$ individual culture passages and transductions, 2 independent experiments). **I,** Experimental outline for **J** and **K**. **J,** Transduced OCI-AML22 xenografts were analyzed 12 weeks after transplantation for the proportion of CD34+CD38− (of BFP+) cells in xenografts: injected (IF) and noninjected femora (nIF). (*continued on next page*)

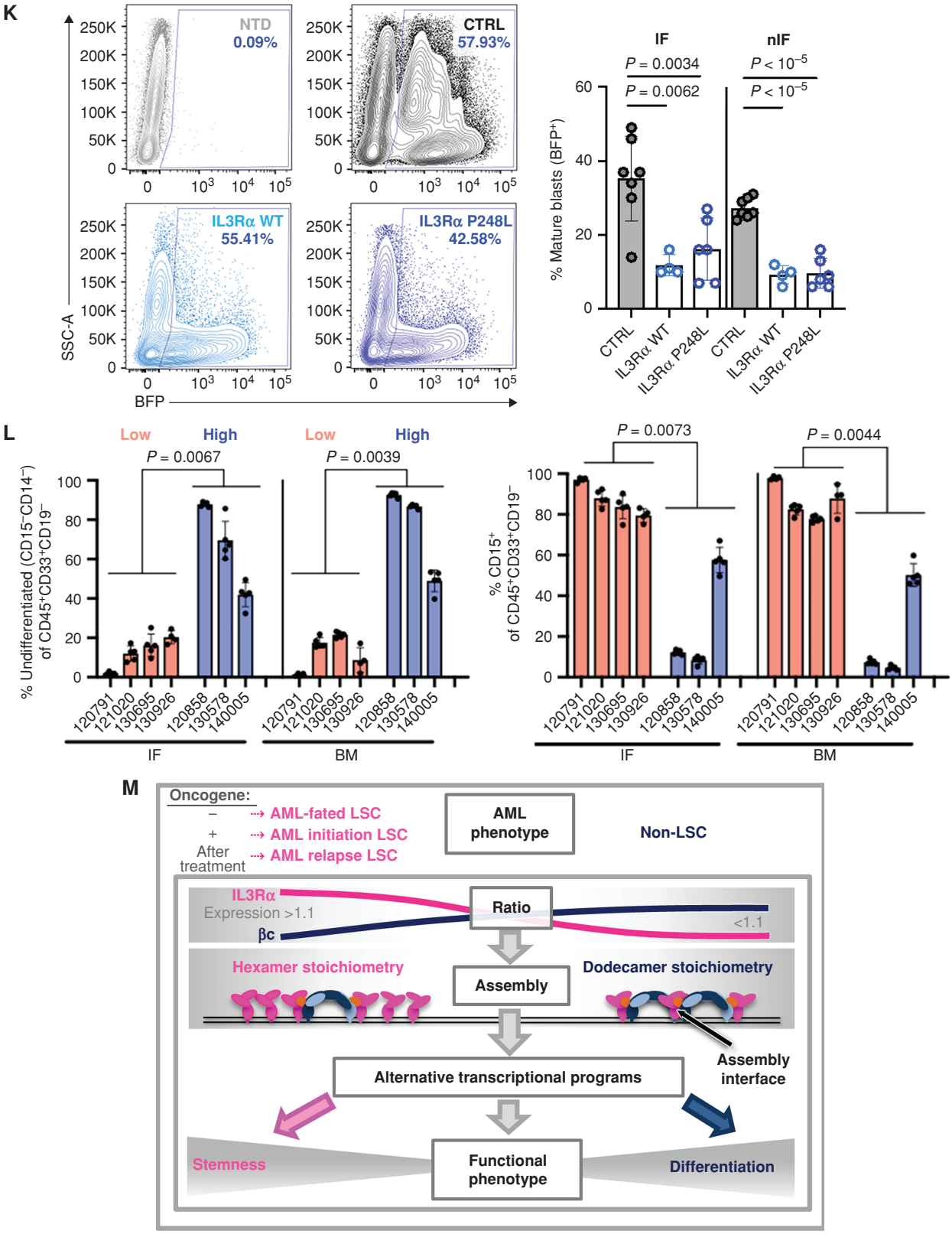

Figure 7. ***(Continued)*** **K,** Representative flow plot showing the lack of a BFP+ mature blast (SSC^{hi}) population (of human CD45+) in IL3Rα WT (high IL3Rα/βc ratio) and IL3Rα P248L (hexamer) xenografts, with quantification of the population shown on the right. NTD, N-terminal domain. **L,** Flow cytometric analysis of CD15 and CD14 expression in primary AML patient xenografts (63) with high (indicated in blue) vs. low (indicated in pink) IL3Rα/βc gene expression ratio ($n = 7$ patient samples from Fig. 1D). BM, noninjected bone marrow; IF, injected femur. **M,** Model of how the IL3Rα/βc ratio and IL3R hexamer stoichiometry dictate LSC emergence, initiation, and relapse in AML.

DISCUSSION

Here, we reveal a new mechanism of pleiotropy by which varying cytokine receptor stoichiometries drive distinct assemblies. This discovery provides the missing link that explains how pleiotropy can influence selective signaling, gene expression programs, and cell-fate outcomes. Our study establishes that (i) the stoichiometry of IL3R subunits is biologically relevant in mediating unique signaling and biological outcomes downstream of IL3R, and (ii) a high IL3Rα versus βc ratio biases for hexamer formation, which drives a stemness-promoting gene expression program (Fig. 7M). More broadly, we suggest a model whereby the stoichiometry of heterodimeric receptors and its resultant differential cytokine signaling mechanisms regulate cell fate in an analog rather than digital fashion, with the ratio of receptor subunits across the individual cell types that occur in a cellular hierarchy ultimately determining alternative transcriptional programs that drive distinct phenotypes (Fig. 7M).

The finding that a high IL3Rα/βc ratio leads to stemness may be generalizable and particularly relevant to cancers expressing pathogenic mutations where an abnormal ratio may act as a permissive gate to enable transformation and oncogenesis. In the case of AML, this perturbation of the balance between cell-fate decisions is critical when leukemogenic processes are initiated in the cell of origin and in ultimately defining the hierarchical organization of the resulting AML. Similarly, because different leukemic blast populations with active stemness gene expression programs can emerge in AML at relapse (21, 64), our prediction is that LSCs with a high IL3Rα/βc ratio and active hexamer signaling reside in a latent, chemoresistant quiescent state and later transition to promote proliferative outgrowth and disease recurrence (Fig. 7M). Our study raises the question of how these variations in expression levels arise. Leukemogenic mechanisms such as *RUNX1* mutations may upregulate IL3Rα expression at the LSC or leukemic progenitor cell stage, thus biasing cells to hexamer IL3R signaling. Alternatively, elevated IL3Rα expression may be epigenetically driven and reflect the levels seen in the cell of origin as a prerequisite for initiating leukemogenesis. Indeed, whether biased signaling is ultimately involved in promoting leukemic transformation or rather plays a role in propagating the disease might strongly depend on the cell of origin in the individual AML. The mechanisms that drive the downregulation of βc expression are also of emerging interest as we have shown that either an increase in IL3Rα expression, a decrease in βc expression, or both actively drives significant alterations to the IL3Rα/βc ratio (Supplementary Fig. S1A).

Our study has revealed alternative cytokine receptor assemblies as a fundamental mechanism underlying biased signaling, altering the balance between STAT5 and STAT1 phosphorylation, to dictate cell fate. STAT5 signaling has been shown to be critical for stemness and self-renewal (65–70), whereas STAT1 signaling has been implicated in monocytic differentiation and macrophage maturation (50, 51). Importantly, disrupting the balance between STAT5, STAT1, and STAT3 signaling can alter differentiation kinetics and cell fate in normal hematopoiesis (6, 71) and in hematologic diseases (72). We postulate that different receptor assemblies alter the balance between STAT5 and STAT1 signaling. At high IL3Rα/βc ratios, in the absence of STAT1 phosphorylation, STAT5 signaling is predominant and induces a prostemness response. However, as the IL3Rα/βc ratio approaches 1:1, STAT1 signaling emerges to stimulate prodifferentiation effects. Revealing the underlying transcription factor networks that regulate the balance between different STATs will provide important insights into the mechanisms that control cytokine-regulated stemness.

Our observations that the IL3Rα/βc ratio in AML cells is higher than that found in normal HSPCs (Fig. 1F; Supplementary Fig. S1K) and that IL3Rα is elevated regardless of mutational subtype heterogeneity in >90% of patient samples led us to propose that the increase of the IL3Rα/βc ratio in malignancy is a unifying mechanism for further biasing toward hexamer assembly and signaling regardless of mutation. The end result is an elevation of stemness and a block of differentiation—canonical characteristics of AML. The impact of alternative IL3R assemblies as a fundamental mechanism for stemness versus differentiation is supported by several recent studies that have highlighted the heterogeneity of the composition of the cellular hierarchy between patients with AML (31, 32, 35, 73). Stratification of patients with AML based on their hierarchy composition is emerging as clinically significant, as it is highly predictive of patient survival outcomes and response to conventional and investigational therapies, with potential applications extending to monitoring of disease progression and relapse (31, 32). Thus, monitoring elevated IL3Rα/βc ratios might reveal early leukemogenic events and have the potential for biomarker development to capture both disease onset and relapse in AML. Moreover, the identification of therapeutic targets that enforce IL3R dodecamer assembly to induce LSC differentiation represents a novel avenue for therapy development in AML. In fact, engineered cytokine ligands that elicit biased signaling and functional outcomes are emerging as promising therapeutics (9, 74, 75). While this approach has focused up to now on altering affinities for receptor, or geometries between receptor subunits, our findings unlock the potential of modulating receptor assembly through rational design of biased agonists of the assembly interface as novel cytokine therapeutics to alter cell fate. As receptor stoichiometries vary between different cell types, engineered agonists should take into consideration receptor expression levels and stoichiometries on the target cell to promote specific receptor assemblies and dictate different biological outcomes. This could be taken advantage of for fine-tuning the rational design and development of biased cytokine therapeutics with enhanced specificity for the target cell type while preventing activation of other cell types to eliminate off-target effects and toxicities.

In summary, our results provide a paradigm shift for understanding how pleiotropy arises from a single ligand–receptor pair. Our results may be generalizable to many cancer types that are similarly driven by stemness and transformed cellular hierarchies and suggest that altered receptor expression may play a role in the disease not simply by mediating excessive signaling (e.g., overexpressed *HER2* in breast cancer) but also by biasing pleiotropic signaling at the cell surface through distinct forms of assemblies of heteromultimeric receptors.

METHODS

Cell Lines

HEK293T (RRID: CVCL_0063) and COS-7 (RRID: CVCL_0224) cells sourced from the ATCC were cultured in DMEM with 10% fetal bovine serum (FBS) and antibiotics. FDH cell lines were generated by transduction of embryonic day 14.5 (E14.5) fetal liver cells from mice lacking βc and β_{IL3} (76) immortalized using a pFTREtight MCS rtTAadvanced GFP lentivirus encoding a doxycycline-inducible HOXA9-FLAG expression cassette (45) as previously described (47) and are maintained in Iscove's modified Dulbecco's medium (IMDM) supplemented with 10% FBS, antibiotics, 100 ng/mL murine SCF (produced in-house; ref. 47), and 0.5 μg/mL doxycycline hyclate (Sigma-Aldrich #D9891). Cell lines were not tested for *Mycoplasma* contamination, and experiments were performed on cells 5 to 20 passages after thawing.

Determination of IL3Rα and βc Expression in AML Patient Specimens

Gene expression measurements in tabular count format for 451 specimens from 411 patients were retrieved from the Beat AML Functional Genomic Study (ref. 26; Fig. 1A). IL3Rα and βc gene expression data [reads per kilobase per million mapped reads (RPKM) range, 2.01–10.17 and 1.67–10.50, average: 6.7 and 6.5 for *IL3RA* and *CSF2RB*, respectively] were used to stratify patients into IL3Rα/βc-high and IL3Rα/βc-low groups based on upper (RPKM $\log_2$ fold change >0.31; $n = 113$) and lower ($\log_2$ fold change < −0.27; $n = 113$) quartile thresholds, respectively. Differential expression analysis between the two resulting groups was carried out using GSEA as described below.

For patient survival analyses, we analyzed two independent normal karyotype AML cohorts [The Cancer Genome Atlas (TCGA); ref. 25, and Beat AML; ref. 26] split into high ratio (IL3Rα>βc, facilitating hexamer formation) versus low ratio (IL3Rα<βc, dodecamer assembly; Fig. 1B; Supplementary Fig. S1A). We applied a ratio cutoff of 1.1 for IL3Rα/βc based on the highest HR for decreased overall survival after comparing the log-rank statistic with all possible ratio cutoffs, binning at 0.1. Kaplan–Meier overall survival curves for patients with normal karyotype AML from TCGA ($n = 184$) and Beat AML ($n = 102$) were generated comparing those with higher or lower than 1.1 ratio of IL3Rα/βc expression. Similarly, Kaplan–Meier overall survival curves were generated for a 1.12 ratio of *CSF2RA* versus *CSF2RB* of the GM-CSF receptor and a 3.5 ratio of *IL6R* versus *IL6ST* of the IL6 receptor for the TCGA cohort (Supplementary Fig. S1D and S1E).

For single-cell analyses of IL3Rα and βc gene expression in AML, we obtained single-cell RNA-seq data from diagnostic AML samples of 12 patients (35) and applied scran normalization (77) to the raw count data. For each malignant cell type, we depicted the mean expression of the IL3Rα and βc transcripts. Transcriptional profiling of cells with LSPC-quiescent, LSPC-primed, LSPC-cycle, and monolike signatures was determined and scored according to ref. 32. For analysis comparing gene expression between LSC^+ and LSC^- AML fractions, we used normalized microarray data with functional LSC annotations from ref. 20 (GSE76009); IL3Rα, βc and IL3Rα/βc gene expression values between LSC^+ and LSC^- fractions were compared with a Mann–Whitney test (two-tailed).

Primary AML Samples for Immunophenotypic and Transcriptional Profiling and Sorting (Toronto Cohort)

All biological samples were collected with written informed consent according to procedures approved by the Research Ethics Board of the University Health Network (UHN; REB# 01-0573-C), and AML patient samples and mobilized peripheral blood from a healthy donor were viably frozen in the Leukemia Tissue Bank at Princess Margaret Cancer Centre (Toronto, Ontario, Canada). The UHN Research Ethics Board operates in compliance with the Tri-Council Policy Statement; International Council for Harmonisation Guideline for Good Clinical Practice E6(R1); Ontario Personal Health Information Protection Act (2004); Part C Division 5 of the Food and Drug Regulations; and Part 4 of the Natural Health Products Regulations and the Medical Devices Regulations of Health Canada. Human CB samples were obtained from Trillium and Credit Valley Hospital and William Osler Health Centre, processed as previously described, and stored viably as mononuclear cells (MNC) at −150°C (38). The inclusion criteria for AML samples were either a high ($n = 5$; >1) or a low ($n = 5$; <1) IL3Rα/βc transcript ratio according to previously obtained RNA-seq data. The IL3Rα/βc ratio was 2.72 ± 1.83, $n = 5$, in the high-ratio samples, whereas the ratio was 0.67 ± 0.23, $n = 5$, in the low-ratio samples ($P = 0.038$). Samples were thawed by dropwise addition of X-VIVO + 50% FBS supplemented with DNase (100 μg/mL final concentration, Roche) and resuspended in PBS + 5% FBS for antibody staining at a cell density $<10^7$/mL. All samples were stained (i) with anti–CD123-PeCy5 (BD #551065, RRID: AB_394029), anti–CD131-PE (BioLegend #306104, RRID: AB_2085808), anti–CD45-V450 (BD #560367, RRID: AB_1645573), anti–CD3-FITC (BD #349201, RRID: AB_400405), anti–CD19-AF488 (BD #55769, RRID: AB_396806), and Fixable Viability Dye eFluor 506 (eBioscience #65-0866-14) for immunophenotypic analysis on a Sony SH800 instrument or (ii) for additional immunophenotypic characterization with anti–CD45-V500 (BD Biosciences #560777, RRID: AB_1937324), anti–CD33-BV421 (BioLegend #303416, RRID: AB_2561690), anti–CD34-APCCy7 (BD, custom-made, #624072), anti–CD38-BV711 (BD #563965, RRID: AB_2738516), anti–CD36-FITC (BD #555454, RRID: AB_2291112), anti–CD3-PC5 (Beckman Coulter #IM2635U, RRID: AB_10645166), anti–CD19-PC5 (Beckman Coulter #IM2643U, RRID: AB_131160), and anti–CD123-PE (for IL3Rα; BD #555644, RRID: AB_396001) or CD131-PE (for βc; BioLegend #306104, RRID: AB_2085808), and 7AAD (BD #559763, RRID: AB_2869265) was used for live/dead discrimination on a BD Celesta. Subsequent analysis was performed with FlowJo 10.7.1. Statistical significance was determined by one-way ANOVA with Tukey posttest. An unpaired *t* test (two-tailed) was used for Supplementary Fig. S1I and S1M. Samples AML#140005 and AML#130578 were also stained with anti–CD45-AF700 (BD #560566, RRID_AB_1645452), anti–CD3-FITC (BD #349201, RRID_AB_400405), anti–CD19-AF488 (BD #557697, RRID: AB_396806), anti–CD131-PE, and anti–CD123-PeCy5, and SytoxBlue (Thermo Fisher #S34857) was used for live/dead discrimination for sorting on a FACSAria II (BD Biosciences).

Primary AML Samples for Immunophenotypic Profiling (Adelaide Cohort)

Apheresis product or bone marrow samples were obtained from patients diagnosed with AML and retrieved from the South Australian Cancer Research Biobank with written informed consent according to institutional guidelines, and studies were approved by the Central Adelaide Local Health Network Human Research Ethics Committee (CALHN HREC #HREC/15/RAH/448) and conducted in accordance with the Declaration of Helsinki. The CALHN HREC is constituted in accordance with the National Health and Medical Research Council National Statement on Ethical Conduct in Human Research 2007 (updated in 2018) and is accredited under the National Mutual Acceptance Scheme. MNCs from bone marrow or apheresis product samples were isolated by Ficoll-Hypaque density-gradient centrifugation and resuspended in IMDM containing 10% FBS. The inclusion criteria for AML samples were either a high ($n = 5$; >1.1) or a low ($n = 6$; <1.1) IL3Rα/βc ratio according to previously obtained RNA-seq data. The IL3Rα/βc ratio was 1.50 ± 0.12, $n = 5$, in the high-ratio samples, whereas the ratio was 0.73 ± 0.021, $n = 6$, in the low-ratio samples ($P < 0.0001$, unpaired *t* test, two-tailed).

Samples were thawed by dropwise addition of IMDM + 20% FBS supplemented with DNase (50 U/mL) and penicillin/streptomycin. After overnight incubation in IMDM + 10% FBS + IL3, TPO, SCF, FLT3L, and IL3, cells were resuspended in PBS + 2% FBS (3×10^5 cells/stain) and stained with anti–CD123-BV480 for IL3Rα (BD #566133, RRID: 2739532), anti–CD131-BV421 for βc (BD #564192, RRID: AB_2738659, anti–CD34-PE (BD #550761, RRID: AB_393871), anti–CD38-BUV395 (BD #563811, RRID: AB_2744372), and Fixable Viability Stain 780 (BD #565388) for 30 minutes on ice. After washing, cells were resuspended at $0.5–2 \times 10^6$ cells/mL in PBS and 2% FBS, followed by immunophenotypic analysis and determination of %IL3Rα^{hi}/βc^{lo} cells and IL3Rα/βc ratio on BD LSRFortessa (BD Biosciences). Subsequent analysis was performed with FCS Express 6 (De Novo Software). Statistical significance was determined by an unpaired *t* test (two-tailed; Supplementary Fig. S1J) and two-way ANOVA with a Tukey post hoc analysis (Supplementary Fig. S1L).

Expression and Purification of the IL3R Ternary Complex

We prepared an IL3R ternary complex using partially glycosylated variants of the IL3Rα and βc extracellular domains and a truncated IL3 as previously described (47). DNA fragments encoding soluble IL3Rα ΔN5 (sIL3Rα; residues L20–S307 of the expressed peptide with the N212Q mutation) or soluble βc ΔN3 (sβc; residues E25–T436 of the expressed peptide with the N346Q mutation) were cloned into the pFastBac1 vector (Invitrogen). The resulting plasmids were transformed into the DH10Bac *Escherichia coli* strain from which recombinant bacmid DNA was isolated and used to transfect Sf9 insect cells to produce recombinant viral particles (78). The sIL3Rα ΔN5 and sβc ΔN3 proteins were expressed from infected Sf9 cells and immunoaffinity-purified as previously described (78, 79). Human IL3, comprising residues Y13–Q125 of the mature peptide with a W13Y mutation and a GAMGS N-terminal tail arising from the expression plasmid, was expressed and purified from *E. coli* as a NusA fusion protein and cleaved with TEV protease, and the IL3 recovered (80).

A ternary complex consisting of IL3, sIL3Rα ΔN5, and sβc ΔN3 was isolated by size exclusion chromatography (SEC) of a 2:1.5:1 molar ratio mixture of IL3:sIL3Rα ΔN5:sβc ΔN3. SEC was performed using a Superdex 200 column (26 mm × 600 mm, GE HealthCare) operated at 2 mL/min at 4°C with 150 mmol/L NaCl and 50 mmol/L sodium phosphate pH 7.0 as running buffer.

Crystallization and Data Collection

Prior to screening for suitable crystallization conditions, the IL3–IL3Rα–βc complex was buffer-exchanged to 20 mmol/L sodium citrate pH 6.5 buffer containing 50 mmol/L sodium chloride and concentrated to 10 mg/mL. Several crystallization screens were tested including JCSG+, PACT, Hampton PEG/Ion, and Hampton at 4°C and 21°C. Small rod-shaped crystals were obtained in 0.2 M magnesium chloride, 10% polyethylene glycol (PEG) 8000, and 0.1 M Tris pH 7 at 21°C from the JCSG+ screen. Crystals were optimized using the hanging drop vapor diffusion method and cryoprotected in 30% ethylene glycol. X-ray data were collected at the MX2 beamline at the Australian Synchrotron using Blue-Ice software (81, 82). The crystals belonged to the $P2_12_12_1$ space group with unit cell dimensions of $a = 111.6$ Å, $b = 157.3$ Å, $c = 168.3$ Å. Data were integrated using XDS (83) and scaled using Aimless (84).

Structure Determination

The structure was solved by molecular replacement using Phaser (85) with search models, including domains D1 to D4 of βc, D2 to D3 of βc [Protein Data Bank (PDB) ID: 4NKQ; ref. 40], and the IL3 cytokine (PDB ID: 1JLI; ref. 86). A partial solution was obtained (Translation Function Z-score of 7.2), consisting of two copies of the βc homodimer containing domains D1, D2, D3, and D4 and two copies of the cytokine. Using this model from Phaser, the IL3Rα domains N-terminal domain (NTD), D2, and D3 were manually built into strands of density around the two cytokines by repeated rounds of manual building in COOT (87), followed by restrained refinement using REFMAC 5 (88). The final model consists of two copies of the IL3R ternary complex positioned adjacent to each other in the asymmetric unit cell. The two molecules in the asymmetric unit superimpose closely with root-mean-square deviation (RMSD) of 1.0 Å for all Cα atoms. The final model consists of two copies of IL3 (chain I, residues: Y13–A121 and chain J, residues: Y13–N120), two copies of IL3Rα (chain F, residues: P26–Q295 and chain M, residues: T28–Q295 but missing residues 46–48 and 90–92 due to poor electron density) and two copies of a partial βc homodimer consisting of chains A (residues E25–P239) and B (residues D241–T436) from dimer 1 and chains C (residues E25–P239) and D (residues D241–E437) from the βc dimer 2. The IL3R ternary complex has glycosylation sites on IL3Rα residues N64, N80, and N218 on chain F, residues N218 and N80 on chain M, as well as N58 on βc chains A and C. The stereochemical quality of the final model correlates well with other structures of similar resolution, with 99.7% residues in the allowed regions of the Ramachandran plot. Data and refinement statistics are listed in Supplementary Table S1. The PISA (Protein Interfaces, Surfaces, and Assemblies) server (http://www.ebi.ac.uk/msd-srv/prot_int/pistart.html) was used for all protein–ligand surface interaction calculations. The PyMOL Molecular Graphics System, Version 1.8.2.2 (Schrodinger, LLC; http://www.pymol.org), was used to visualize and analyze the protein structures and generate figure images. Atomic coordinates and structure factors have been deposited in the PDB under the ID code 6NMY.

Structural Analysis of the IL3R Ternary Complex

In the asymmetric unit, there are two copies of IL3 (i.e., IL3, IL3'), two copies of IL3Rα (i.e., IL3Rα, IL3Rα'), and two copies of a partial βc homodimer consisting of domains D1 and D2 from the first βc homodimer and domains D3 and D4 from the second βc' homodimer (Fig. 2A).

The overall architecture of the IL3–IL3Rα complex within the ternary crystal structure (Supplementary Fig. S2A) is almost identical to the crystal structure of the isolated IL3–IL3Rα binary complex (PDB ID: 5UV8; ref. 47), with an RMSD of 0.7 Å via the IL3Rα Cα atoms. The total buried surface area for site 1a and site 1b is ~1161 Å^2. Recruitment of the βc homodimer to the IL3–IL3Rα binary complex through sites 2 and 3 (Fig. 2B; Supplementary Fig. S2B) results in the formation of a high-affinity complex and is critical for cytokine-mediated activation of the receptor. The buried surface area at the site 2 interface is ~584 Å^2, and the interactions are mediated by polar residues on IL3 helices A and C, forming hydrogen bonds with residues spread across a noncontiguous interface composed of the AB and EF loops of D1 from one βc monomer and the BC and FG loops of D4 from the other βc monomer. In addition to the conserved interaction between IL3 E22 and βc Y421 (89, 90), the site 2 interface is stabilized by several polar contacts involving N18, E22, H26, Q29, S76, and N80 on IL3 (Supplementary Fig. S2B; Supplementary Table S2). The site 3 interface buried surface area is ~830 Å^2, and it is stabilized predominantly by the formation of electrostatic interactions involving charged IL3Rα D3 residues on β-strands C, D, and E and the DE loop (Supplementary Fig. S2B; Supplementary Table S2). On D4 of βc, site 3 interactions are mediated by residues on the AB loop (D350–S353), residues on the BC loop (E366–H370), and residues on the short D β-strand, as well as S417 and R418 on the FG loop. The buried surface area at the "assembly interface" is ~450 Å^2, and the interactions are mediated by the formation of 8 hydrogen bonds. In contrast, interactions between G351 residues (not shown in Fig. 2C) on adjacent βc subunits (i.e., βc–βc') contribute only ~46 Å^2 to the "assembly interface" and are driven by Van der Waals forces (Fig. 2C). Cytokines from adjacent hexamers interact to form the bulk of the site 5 interface, with additional interactions between the

30-PPLPLL-35 motif in the IL3 AB loop and βc' D2 from adjacent hexamers (Supplementary Fig. S2C). Site 5 is a membrane distal interface of ~359 Å^2 located directly above "assembly interface," and the formation of this site is driven predominantly by a network of 11 hydrogen bonds between IL3 helices C and D involving residues Q69, N70, D103, W104, and N105 (Supplementary Fig. S2D).

Assembly of the IL3R dodecamer is reminiscent of the related GM-CSF receptor dodecamer (PDB ID: 4NKQ; refs. 13, 40), but in the latter, significant differences in the βc subunit D1–D4 hinge angles alter the extent of arching in the βc homodimer, and the equivalent "assembly interface" (site 4) is primarily between βc membrane-proximal domains from adjacent hexamers (i.e., βc–βc'; Supplementary Fig. S2E), whereas the "assembly interface" interaction in IL3R is predominantly between the membrane-proximal domains of βc and IL3Rα (Fig. 2C; Supplementary Fig. S2E). This marked difference between the site responsible for higher-order complex assembly in the IL3 and GM-CSF receptor complexes may contribute to the well-known but unexplained different pleiotropic effects of IL3 and GM-CSF (91). Despite this, the buried surface area at the "assembly interface" in the GM-CSF receptor dodecamer (i.e., site 4) is comparable to the equivalent buried surface area in the IL3R dodecamer (site 1: 1133 Å^2, site 2: 571 Å^2, site 3: 822 Å^2, Assembly interface: 498 Å^2, site 5: 359 Å^2).

FLIM-FRET Analysis of Receptor Subunit Assembly

For experiments shown in Fig. 2D and E, genes for the SYFP2 L68V (pSYFP2-C1, #22878) and mScarlet-I (pmScarlet-I_C1 #85044; ref. 92) fluorescent proteins were obtained from Addgene. A synthetic DNA fragment encoding a fusion protein of the viral 2A peptide linker (EGRGSLLTCGDVEENPGPGS; ref. 59), V2 to S505 of βc and the mCerulean fluorescent protein, was obtained from Geneart (Thermo Fisher). Using an overlap extension PCR strategy, cDNA fragments encoding M1 to T378 of WT and P248L forms of IL3Rα were fused via a GGGS linker with V2 to K238 of SYFP2, V2 to K231 of mScarlet-I, or V2 to K239 of mCerulean. The resulting fragments were subcloned into the retroviral expression vector pRufHygro to create pRufHygro:IL3Rα–SYFP2, pRufHygro:IL3Rα–mScarlet-I, and pRufHygro:IL3Rα–mCerulean. A cDNA fragment encoding M1 to S505 of βc was fused, using a similar approach, via a GGGS linker with V2 to K238 of SYFP2. The resulting fragment was subcloned into the retroviral expression vector pRufPuro to create pRufPuro:βcS505–SYFP2. We truncated the βc cytoplasmic domain at S505 to ensure that the C-terminally fused mScarlet-I protein was located at approximately the same distance from the cell membrane as the C-terminally fused SYFP2 protein on IL3Rα. For expression of untagged βc, we cloned truncated βcS505 into pRufPuro to create pRufPuro:βcS505.

HEK293T cells (1×10^6 cells/25 cm^2 flask) were transfected with combinations of 1 μg of the pRufHygro:IL3Rα plasmids or 5 μg of the pRufPuro:βc plasmids described above using Lipofectamine 2000 (Invitrogen #11668019). Transfected HEK293T cells were plated in 500 μL DMEM in a 35-mm imaging dish (Ibidi) at 1×10^5 cells per dish 24 hours after transfection. After a further 24-hour incubation, FLIM-FRET analysis (93) was performed by live-cell imaging using confocal microscopy on a Leica TCS SP8 equipped with environmental control, a pulsed white light laser (WLL), and an SMD/FLIM module and Symphotime software (PicoQuant). Live-cell FLIM images (512 × 512 pixels at 2.6 pixels/μm) of SYFP2 in the presence or absence of FRET acceptors were acquired at 37°C using an HC PL APO CS2 40× water objective, scan speed 400, and pinhole set to 1 AU. For analysis of Time-Correlated Single Photon Counting (TCSPC), the wavelength and pulse frequency of the WLL were set at 514 nm and 20 MHz, respectively. Fluorescence emission was collected between 525 and 560 nm. For measurements of lifetime, 60 frames were acquired per field for the generation of TCSPC histograms that were then used to determine SYFP2 fluorescence lifetime by fitting these to mono-decay models in the region outside the instrument response in the histogram. For these measurements, we used TCSPC resolution set to 8 ps within the Symphotime software. After the acquisition of FLIM data, images of the FRET donor and acceptor were acquired using the same optical path using exc 514 nm/em 525 to 560 nm for SYFP2 and exc 569/em 575 to 611 for mScarlet-I.

For the different conditions, FLIM analysis was performed on regions of interest (ROI) drawn at the plasma membrane of cells (identified by either mScarlet-I or SYFP2 fluorescence). TCSPC histograms were obtained for each ROI and fitted to obtain a fluorescence lifetime value. For each experiment, we took eight images corresponding to eight fields with 20 ROIs/field (one ROI per cell). These experiments were repeated at least three times, as indicated in the figure legends (Fig. 2D and E), and Supplementary Fig. S3G–S3I show mean SYFP2 lifetimes from a representative experiment that were used to calculate %FRET efficiencies. Values are shown as mean ± standard error of the mean (SEM). Statistical significance was determined by an unpaired *t* test (two-tailed).

For IL3Rα–βc FLIM-FRET experiments (Fig. 7B; Supplementary Fig. S6A and S6B), an overlap extension PCR subcloning strategy was used to fuse βcS505–SYFP2 to a synthetic viral 2A–βcS505–mCerulean fragment (Geneart). The resulting fragment was subcloned into pRufBlast to create pRufBlast:βcS505–SYFP2–2A–βcS505–mCerulean. HEK293T cells were transfected with different combinations of 0.5 to 5 μg of pRufHygro:IL3Rα–mScarlet-I and 5 μg of pRufBlast:βcS505–SYFP2–2A–βcS505–mCerulean as described above.

For βc–βc' FLIM-FRET experiments (Fig. 7C; Supplementary Fig. S6C and S6D), an overlap extension PCR subcloning strategy was used to fuse βcS505–SYFP2 to a synthetic viral 2A–βcS505 fragment and the mScarlet-I fluorescent protein. The viral 2A peptide linker was used to enable equimolar coexpression of βcS505–SYFP2 and βcS505–mScarlet-I. The resulting fragment was subcloned into pRufPuro to create pRufPuro:βcS505–SYFP2–2A–βcS505–mScarlet-I. HEK293T cells were transfected with different combinations of 0.5 to 5 μg of pRufHygro:IL3Rα–mCerulean and 5 μg of pRufPuro:βcS505–SYFP2–2A–βcS505–mScarlet-I as described above.

After a further 24-hour incubation, FLIM-FRET analysis was performed by live-cell imaging using confocal microscopy using the methods described above. After the acquisition of FLIM data, images of the FRET donor (SYFP2), acceptor (mScarlet), and mCerulean were acquired using the same optical path using exc 405 nm/em 460 to 500 nm for mCerulean, exc 514 nm/em 525 to 560 nm for SYFP2, and exc 569/em 580 to 610 for mScarlet-I. The mCerulean, mScarlet-I, and SYFP2 fluorescence on ROIs drawn at the cell membrane was quantified to determine the expression of receptor units. In the FLIM-FRET schematic diagram shown in Fig. 7A, the mCerulean fluorophore is not shown, as it was used for quantifying receptor expression levels on the cell surface, but not for FLIM donor lifetime measurements. For the different conditions, FLIM analysis was performed on ROIs drawn at the plasma membrane of cells (identified by either mCerulean, mScarlet-I, or SYFP2 fluorescence). TCSPC histograms were obtained for each ROI and fitted to obtain an SYFP2 fluorescence lifetime value. For each experiment, we took 20 images corresponding to 20 fields with approximately 20 ROIs/field (one ROI per cell). FLIM donor lifetimes were converted into %FRET efficiencies using the formula: [1 − (donor lifetime in the presence of acceptor/donor lifetime in the absence of acceptor)] × 100. For each experiment, 400 cells per condition were analyzed, and the average donor lifetime was measured. %RET efficiency values were plotted as a function of the IL3Rα/βc ratio binned at 0.1 IL3Rα/βc fluorescent ratio units, taking only those bins containing >3 ROIs (MATLAB, Mathworks), averaged across $n = 3$ independent experiments and shown as mean ± SEM (Supplementary Fig. S6A and S6C). For Fig. 7B and C, %FRET efficiencies were measured and plotted based on the top and bottom 50% of IL3Rα/βc expression ratio (in fluorescence units)—that is, high- and low-ratio groups, respectively. The mean %FRET efficiencies of the top and bottom IL3Rα/βc expression groups were calculated for each experiment, were averaged across three independent experiments, and are shown as

mean ± SEM. The IL3Rα/βc ratio of the high- and low-ratio groups of all of the experimental conditions (mean ± SEM for $n = 3$ independent experiments) is shown in Supplementary Fig. S6B and S6D. Statistical significance was determined by two-way ANOVA, with the Sidak post hoc multiple comparisons test.

Cell-Surface IL3 Binding and IL3R Stability Assays

Saturation binding assays were performed on transfected COS-7 cells to assess low-affinity binding or FDH cell lines expressing IL3R (βc + IL3Rα P248L) hexamers or (βc + IL3Rα WT) dodecamers to assess high-affinity binding using radioiodinated IL3 as previously described (90, 94). COS-7 cells were electroporated with pSG5:IL3Rα plasmids encoding WT or mutant IL3Rα. Cell-surface expression of receptor subunits was confirmed by flow cytometry. IL3 was radioiodinated with ^{125}I (PerkinElmer) using Pierce Precoated Iodination tubes (Thermo Scientific; refs. 47, 80). Dissociation constants were calculated using the EBDA and LIGAND programs (KELL Radlig; ref. 95). Statistical significance of differences in K_D values between cells expressing WT or IL3Rα (P) was determined using a two-tailed unpaired t test. To assess the stability of IL3Rα P248L compared with WT IL3Rα at the cell surface, all cell-surface proteins were biotinylated according to a commercially available kit (Pierce, #S44390) in FDH cells expressing P248L or WT IL3R at 0 to 60 minutes after IL3 stimulation, followed by streptavidin pulldown enrichment and immunoblotting of pulldowns for IL3Rα using anti-IL3Rα 9F5 antibody.

Generation and Testing of IL3R Hexamer Mutants in FDH Cell Lines

To investigate the functional role(s) of the IL3R hexamer, we performed mutations of residues in the "assembly interface" (Supplementary Table S2) in IL3Rα or βc and introduced them into FDH cells, an established murine model of granulocyte–macrophage progenitor cell growth and differentiation lacking expression of mouse βc and β_{IL3} (47). Human IL3Rα and βc cDNAs were cloned into the pSG5 (Stratagene) expression vector and "assembly interface" mutations generated by PCR (94). WT and mutant IL3Rα cDNA were subcloned into the retroviral expression vector pRufHygro and the pRufHygro:IL3Rα plasmids and cotransfected into HEK293T cells with the pEQ-Eco packaging plasmid (96) using Lipofectamine 2000 (Invitrogen) to generate recombinant retrovirus. WT and mutant βc cDNA were subcloned into the pRufPuro and pRufBlast retroviral expression vectors and the pRufPuro:βc or pRufBlast:βc plasmids used to generate recombinant retrovirus by the same approach. Retrovirus was harvested, and retroviral transduction of IL3R subunits into FDH cells was performed by the retronectin method as described previously (47). FDH cells were initially transduced to express WT or mutant βc, selected with puromycin (selection 2 μg/mL, maintenance 1 μg/mL) or blasticidin (selection 10 μg/mL, maintenance 5 μg/mL), and sorted for βc expression by flow cytometry using 1C1 antibody (97) versus an irrelevant mouse antibody 1B5 (anti-Giardia IgG_1) isotype control after pools of resistant cells grew out over 7 to 10 days. Subsequently, the FDH βc cells were transduced to express WT or mutant IL3Rα, selected with hygromycin (selection 500 μg/mL, maintenance 250 μg/mL), and sorted for equivalent IL3Rα expression between the two cell lines by flow cytometry using 9F5 antibody (98) versus 1B5 antibody. Analytical flow cytometry was performed on an LSRFortessa, and data were analyzed using FCS Express 6. Sorting was performed on a FACSAria II (BD Biosciences) or a MoFlo Astrios (Beckman Coulter). Cell proliferation was assessed using CellTiter 96 AQ_{ueous} (Promega, #G3581) following the manufacturer's protocol.

FDH Liquid Culture Assays

In FDH cells, HOXA9 expression is undetectable within 3 days following doxycycline withdrawal, allowing measurements of IL3-induced myeloid cell proliferation, survival, and differentiation. FDH cells expressing βc and WT or P248L-mutant IL3Rα were washed twice in PBS and plated in IMDM, supplemented with 10% FBS (v/v), antibiotics, and 100 ng/mL IL3 or SCF in 25 cm^2 flasks at 10^5 cells/flask and incubated for 5 days. Cytospins were prepared (10^5 cells/slide), stained with May–Grunwald (Sigma-Aldrich #MG500) and Giemsa (Sigma-Aldrich #GS500) and typed and quantified as granulocytes, monocytes/macrophages, and myeloid blasts based on morphology. Statistical significance was determined by two-way ANOVA with Sidak post hoc test. Flow cytometric analysis of stemness and cell differentiation markers were monitored after FDH cells were incubated with 100 ng/mL IL3 for 48 hours. Cells were resuspended in PBS + 2% FBS (3×10^5 cells/stain) and stained with anti–CD11b-APC R700 (BD #564985, RRID: AB_2739033), anti–Gr1 (Ly6G/C)-PE (BD #553128, RRID: AB_394644), anti–CD117-PE (BD 553869, RRID: AB_395103), or anti-lineage antibody cocktail-PerCP-Cy5.5 toward mature lineage cell-surface markers CD3e, CD11b, CD45R/B220, TER-119, Ly-6G and Ly-6C, and PE-Sca-1 (BD #561317, RRID: AB_10612020) or their respective isotype controls for 30 minutes on ice. Cells were washed and resuspended at 10^6 cells/mL in PBS and 2% FBS, followed by analysis on BD LSRFortessa and FCS Express 6.0. Statistical significance was determined by an unpaired t test (two-tailed; Fig. 3C–E) and one-way ANOVA with Sidak post hoc test (Supplementary Fig. S3L–S3N). BrdUrd and cell-cycle analysis were performed by incubating cells with 100 ng/mL IL3 for 48 hours and pulsing with 10 μmol/L BrdUrd for 4 hours. Cells were permeabilized, stained with APC-conjugated anti-BrdUrd and 7-AAD (for DNA content according to the manufacturer's protocol; BD #557892), and analyzed by flow cytometry. Statistical significance was determined by two-way ANOVA with the Sidak post hoc test. For cell survival analysis, cells were treated with 100 ng/mL IL3 for 48 hours, followed by IL3 withdrawal for up to 48 hours and analysis with Annexin V–APC (BD #550475) according to the manufacturer's protocol. Statistical analysis was performed using an unpaired t test (two-tailed) at each time point. Gene expression was assessed using quantitative real-time PCR (qRT-PCR). RNA was extracted from 5×10^5 cells/condition using an RNeasy Plus Micro Kit (Qiagen #74034) according to the manufacturer's instructions. Reverse transcription was carried out on 1 μg of total RNA using the QuantiTect RT Kit (Qiagen #205313), which was then diluted 1:10 prior to quantitative qRT-PCR performed in triplicate using the QuantiTect SYBR Green PCR kit (Qiagen #204143) on a Rotor-Gene 6000 series PCR machine (Qiagen). Analysis was carried out using the comparative quantitative feature of the Rotor-Gene software with data normalized to RPLP expression. Oligonucleotide primer sequences for qRT-PCR, all mouse-specific, are available upon request. Statistical significance was determined by an unpaired t test (two-tailed) unless otherwise stated.

Mouse Fetal Liver Colony Formation and Liquid Culture Assays

In accordance with institutional guidelines approved by the University of South Australia Animal Ethics Committee, fetal liver cells from E14.5 mice lacking βc and β_{IL3} (76) were isolated and retrovirally transduced using the retronectin method described above and in ref. 47 to express βc and IL3Rα WT or P248L using pRufPuro constructs for βc and pRufHygro constructs for IL3Rα. The fetal liver cells were maintained in Eagle's minimum essential medium (Sigma-Aldrich) supplemented with antibiotics, 10% FBS, and 100 ng/mL SCF. Subsequently, the transduced cells were sorted for viability using Fixable Viability Stain 780 (BD #565388, RRID: AB_2869673) and for IL3Rα and βc coexpression using PE anti-human CD123 (BD #555644, RRID: AB_396001) and BV421 anti-human CD131 (BD #564192, RRID: AB_2738659) antibodies on a MoFlo Astrios (Beckman Coulter), followed by overnight incubation in SCF at 37°C. For serial replating experiments, cells were washed twice with PBS and plated in methylcellulose (Methocult, STEMCELL Technologies) containing

Eagle's minimum essential medium, supplemented with 10% FBS (v/v), antibiotics, 55 μmol/L 2-mercaptoethanol (Gibco), 100 ng/mL IL3 alone or cytokine cocktail containing SCF (100 ng/mL), FLT3 (100 ng/mL, Shenandoah Biotechnology #100-21), IL6 (50 ng/mL, Shenandoah Biotechnology #100-10), and G-CSF (10 ng/mL, Shenandoah #100-72) in meniscus-free 35-mm wells (SmartDish, STEMCELL Technologies; #27371) at 2,000 cells/well in triplicate. Colonies were quantified and harvested on day 7, triplicates were combined, and 1% of total cells harvested were reseeded in triplicate in IL3 alone or cytokine cocktail. At day 14, colonies were quantified, and the procedure was repeated for a third plating but with 3% of total cells harvested reseeded in triplicate in IL3 or cytokine cocktail. At day 21, colonies were quantified and 20% of the total cells harvested were reseeded in triplicate in IL3 alone or cytokine cocktail for a fourth plating. Total colony number after final replating was assessed on day 28. Statistical significance was determined by two-way ANOVA and the Sidak post hoc test.

For liquid culture assays, cells were washed twice in PBS and plated in Eagle's minimum essential medium, supplemented with 10% FBS, antibiotics, and 100 ng/mL IL3 at 8,000 cells/well for up to 10 days. A Caspase-3 assay (Biotium #10402) was performed for the day 10 cultured cells following IL3 withdrawal according to the manufacturer's instructions. Cells were incubated with mouse Fc block (BD 553141, RRID AB_394656), followed by staining with PerCP-Cy5.5 mouse lineage antibody cocktail and APC anti-mouse CD117 (BD #553356, RRID: AB_398536). Statistical significance was determined by unpaired *t* test (two-tailed). Colony assays were performed as described above using 25% of the day 10 cultured cell mass and incubated in triplicate for 10 days, with the determination of statistical significance by a paired *t* test (two-tailed).

RPPA

FDH cells expressing βc and WT or "assembly interface" mutant M246L/P248L/V249 L IL3Rα were stimulated with 100 ng/mL IL3 for specified time points up to 60 minutes before lysis with CLB1 buffer (Zeptosens, Bayer, prepared in the VCFG) at room temperature and quantified using the Pierce Coomassie Blue (Bradford) Protein Assay Kit. Samples were serially diluted in 10% CLB1:90% CSBL1 buffer (Zeptosens, Bayer, prepared in the VCFG) using a Sciclone/Caliper ALH3000 liquid handling robot (PerkinElmer) and spotted onto ZeptoChips (Zeptosens) in duplicate using a Nano-plotter-NP2.1 noncontact microarray system (GeSIM). Chips were blocked under noncontact conditions for 1 hour with BB1 buffer (Zeptosens) and incubated with prevalidated primary antibodies (1:500, 20 hours) and Alexa Fluor 647 anti-rabbit secondary antibody (1:1,000, 4 hours, #Z-25308; Thermo Fisher Scientific). Chips were read on a Zepto Reader instrument (Bayer), and relative fluorescence intensity was calculated using software version 3.1, with all samples normalized to the background values reported in the secondary antibody-only negative control. Pearson correlation was calculated to confirm replicate pairs were adequately correlated (correlation coefficient >0.9). Data were $\log_2$-normalized, median-centered, and rescaled between 0 and 1 using Formula 1, which represents a vector of antibody responses for a given sample. The RPPA heat map was generated in R using pheatmap.

$$\text{Formula 1} = [[ab - \min(ab)]/[\max(ab) - \min(ab)]] \times ab$$

where *ab* is the fluorescence intensity

Cell Lysis and Immunoblotting

FDH cells expressing βc and WT or P248L IL3Rα were stimulated with 100 ng/mL IL3 for specified time points up to 60 minutes before lysis with NP-40 lysis buffer [1% NP-40 (v/v), 150 mmol/L NaCl, 50 mmol/L Tris-HCl pH 8.0, and 10% glycerol (v/v)] for 20 minutes on ice. Lysates were cleared by centrifugation and immunoblotted with antibodies for pJAK1 (Cell Signaling Technology #3331, RRID: AB_2265057), pJAK2 (Cell Signaling Technology #3771, RRID: AB_330403), pSTAT1 (Tyr701; BD #612233, RRID: AB_399556), pSTAT5 (Cell Signaling Technology #9359, RRID: AB_823649), STAT1 (BD #610185, RRID: AB_397584), pSHC (Cell Signaling Technology #2434, RRID: AB_10841301), SHC (Upstate Biotechnology, Inc., #06-203, RRID: AB_310070), pβcY593 (87), βc (84), and Actin (Chemicon International, Inc., #MAB1501, RRID: AB_2223041) and goat anti-rabbit (Invitrogen #31463, RRID: AB_228333) or goat anti-mouse (Invitrogen #31437, RRID: AB_228295) IgG Fc secondary antibodies. Immunoblots were analyzed using chemiluminescence on a Bio-Rad Chemidoc Touch.

STAT1 shRNA Transduction of FDH Cells

Four MISSION Predesigned mouse STAT1 shRNA lentiviral plasmids in pLKO.1-puro were purchased from Sigma-Aldrich as bacterial glycerol stocks (RefSeq: NM_009283; TRCN0000235839, TRCN0000054924, TRCN0000054925, and TRCN0000054926). The pLKO.3 control shRNA (target sequence GCTGGACAATTTGATGATACA) was used as a control. Lentivirus was produced by cotransfection of pLKO plasmids with pCMV-VSVG and psPAX2 into HEK293T cells as described above and virus production in FDH media. FDH cells expressing dodecameric IL3R (pRufHygro IL3Rα and pRufBlast:βc) were transduced with lentivirus encoding STAT1 or control shRNAs using 4 μg/mL polybrene and selected using 2 μg/mL puromycin (shSTAT1 only). The transduction efficiency of control shRNA was determined by flow cytometric analysis of %GFP$^+$ cells to be ~100%. STAT1 knockdown efficiency was assessed by intracellular flow cytometry with anti–STAT1-AF 647 (BD Phosflow #558560, RRID: AB_647143). shSTAT1_3 (TRCN0000054926; target sequence GCTGTTACTTTCCCAGATATT) and shSTAT1_4 (TRCN0000054924; target sequence CCGAAGAACTTCACTCTCTTA) produced the highest STAT1-specific knockdown (>70%) efficiencies (Supplementary Fig. S4B). Subsequent experiments were performed in FDH cells expressing dodecameric IL3R and transduced with STAT1_3 shRNA, STAT1_4 shRNA, or the control shRNA. Flow cytometric analysis for %CD11b$^+$Gr1$^+$, ΔMFI CD117, and ΔMFI lineage cocktail and qPCR analysis for stemness genes were all performed as above.

OCI-AML22 Immunophenotypic and Functional Assessment In Vitro

OCI-AML22 and OCI-AML8227 cells were derived from the long-term expansion of individual primary AML patient samples (60, 62). Primary AML-derived cell models were not tested for *Mycoplasma* contamination. Experiments were performed on cells five to 50 passages after thawing. OCI-AML22 cells were cultured in X-VIVO 10 (Lonza, BE04-380Q) supplemented with 20% BIT 9500 Serum Substitute (STEMCELL Technologies, 09500), 1× Glutamax Supplement (Thermo Fisher Scientific, 35050061), Primocin 0.1 mg/mL (Invitrogen), SCF (200 ng/mL; Miltenyi Biotec, 130-096-696), IL3 (20 ng/mL; Miltenyi Biotec, 130-095-069), TPO (20 ng/mL; PeproTech, 300-18), FLT3L (40 ng/mL; PeproTech, 300-19 B), IL6 (10 ng/mL; Miltenyi Biotec, 130-093-934), and G-CSF (10 ng/mL; Miltenyi Biotec, 130-093-861). Cells were maintained at a density of 0.8×10^6 cells/mL and passaged every 3 to 5 days in a 96-well, flat-bottom plate. The CD34$^+$ fraction was regularly sorted, or dead cell depletion was performed [EasySep Dead Cell Removal (Annexin V) Kit, Stem Cell Technologies; according to the manufacturer's protocol] to serially expand the cells. The QuantiBRITE assay was performed according to the manufacturer's instructions using anti–CD131-PE or anti–CD123-PE costained with anti–CD34-APC-Cy7 (BD, custom-made) and anti-CD38-BV711. For Phosflow, analysis sorted OCI-AML22 fractions were incubated in their standard medium without IL3 for 40 hours before restimulation with 20 ng/mL IL3 for 30 minutes, followed by the addition of 10 volumes of prewarmed

(37°C) 4% PFA and incubation for 10 minutes at 37°C (water bath). Cells were pelleted, resuspended in PBS with 2% FBS, followed by the addition of 20 volumes of prechilled BD Phosflow Perm Buffer III (BD # 558050), and at least 30 minutes incubation on ice before two wash steps with the addition of 4 to 5 volumes of PBS with 2% FBS. After blocking (1:100 human FcR blocking Reagent, Miltenyi), samples were split and individual antibodies [1:5 pSTAT1-Y701-AF647 (BD #612597, RRID: AB_399880), 1:5 pSTAT5-Y694-AF647 (BD #562076, RRID: AB_11154412)] were added. After incubation (1 hour) on ice, samples were 10× diluted with PBS with 2% FBS, and analyzed on a BD Celesta. Lentiviral transductions were carried out at a cell density of 0.5×10^6 to 0.8×10^6 cells/mL in 96-well, round-bottom plates after 2 days of recovery from FACS for $CD34^+$ cells by adding <1/5 of the volume of 100× concentrated viral supernatant prepared as previously described (38). After 24 hours, a half-medium exchange was performed, and cells were subsequently passaged every 3 to 5 days maintaining a density of 0.8×10^6 cells/mL. Lentiviral constructs used were designed and purchased using VectorBuilder [CTRL: VB201218-1192bbf: IL3RAwt: VB201218-1162vcq: IL3RAmut(P248L): VB201218-1170pys]. BFP, CD34 (APCCy7), CD38 (BV711), CD123 (PeCy5), and CD131 (PE) expression was monitored over 5 weeks of culture by flow cytometry using a BD Celesta. PI-$BFP^+CD34^+CD38^-$ and PI-$BFP^+CD34^+CD38^+$ cells were sorted on either a Sony MA900, a Sony SH800, or a Beckman Coulter MoFlo XDP after anti–CD34-APCCy7 and anti–CD38-PECy7 or -BV711 and propidium iodide (PI) staining for subsequent cell-cycle analysis as described previously (61). Statistical significance was determined using a two-tailed unpaired or paired *t* test or one-way ANOVA with the Tukey post hoc test as applicable.

Xenotransplantation

Animal experiments were performed in accordance with institutional guidelines approved by the UHN Animal Care Committee. Twelve- to 17-week-old male and female NSG-SGM3 mice were sublethally irradiated (225 cGy) 24 hours before intrafemoral injection of transduced OCI-AML22 cells or primary AML fractions. Mice were euthanized 7 to 8 weeks (AML) or 12 weeks (OCI-AML22) after transplant and human cell engraftment in the injected right femur, the noninjected left femur, and spleen was assessed by flow cytometry. For OCI-AML22, human-specific antibodies were used in two panels and 1/10 of each cell suspension: (i) anti–CD45-FITC (BD #347463, RRID: AB_400306), anti–CD131-PE, anti–CD123-PE-Cy5 (BD #551065, RRID: AB_394029), anti–CD34-APC-Cy7, anti–CD38-BV711, and Fixable Viability Dye eFluor 506 or (ii) anti–CD45-FITC, anti–CD117-PE (BD #340529, RRID: AB_400044), anti–CD66-AF647 (BD #561645, RRID: AB_10894001), anti–CD34-APC-Cy7, anti–CD38-BV711, anti–CD11b-PC5 (Beckman Coulter # IM3611, RRID: AB_131151), and Fixable Viability Dye eFluor 506. Flow-cytometric analysis was performed on a BD Celesta. Statistical significance was determined by a two-tailed unpaired *t* test. Primary AML-derived xenografts were stained with anti–CD45-V450, anti–CD33-BV786 (BD #740974, RRID: AB_2740599), anti–CD123-PeCy5, anti–CD131-PE, anti–CD14-BV605 (BD #564054, AB_2687593), anti–CD34-APC-Cy7, anti–CD15-FITC (BD #347423, RRID: AB_400299), and anti–CD19-AF700 (BD #557921, RRID: AB_396942). Flow cytometric analysis was performed on a BD Symphony A1. LSC frequency and statistical significance were calculated by ELDA software (https://bioinf.wehi.edu.au/software/elda/; ref. 99).

Hexamer and Dodecamer Gene Expression Analysis and GSEA and GSVA

FDH cells expressing WT IL3Rα or IL3Rα P248L and βc were washed twice in PBS prior to plating in IMDM, supplemented with 10% FBS (v/v), antibiotics, and 100 ng/mL IL3 in 75 cm^2 flasks at 3×10^5 cells/flask and incubated for 2 or 5 days. RNA was extracted from 10^6 cells/condition using the mirVana miRNA isolation kit (Ambion) with phenol. $PolyA^+$ enriched RNA-seq libraries from 3 biological replicates for each treatment across three time points (0, 2, and 5 days) were multiplexed and sequenced on the Illumina NextSeq 500 platform using the stranded, single-end protocol with a read length of 75. Raw data, averaging 29 million reads per sample, were analyzed and quality checked using the FastQC program (http://www.bioinformatics.babraham.ac.uk/projects/fastqc). Reads were mapped against the mouse reference genome (mm10) using the STAR spliced alignment algorithm (ref. 100; version 2.5.3a with default parameters and –chimSegmentMin 20, –quantMode GeneCounts), returning an average unique alignment rate of 81%. Alignments were visualized and interrogated using the Integrative Genomics Viewer v2.3.80 (101).

Differential mRNA expression analysis was evaluated from Trimmed Mean of M values (TMM)–normalized gene counts using R (version 3.2.3) and edgeR (version 3.3; ref. 102) following protocols as described (103). Only genes with a count per million >3 in more samples than the smallest sample size of one of the groups being compared were retained for further analysis. Differences between IL3Rα P248L and IL3Rα WT groups at each time point were examined by creating nested contrasts as described in the edgeR user's guide, Section 3.3.1 (https://www.bioconductor.org/packages/release/bioc/vignettes/edgeR/inst/doc/edgeRUsersGuide.pdf). Graphical representations of differentially expressed (DE) genes were generated using Glimma (ref. 104; Fig. 5B; Supplementary Fig. S4E).

Gene ontology enrichment of significant DE candidates was performed using DAVID (105). The GSEA software package (GSEA v4.1.0) was used to look for coordinate expression to groups of genes in the Molecular Signatures Database (MSigDB v7.1; refs. 106, 107) or against custom-built gene sets. Genes were ranked for the GSEA (GSEAPreranked) by calculating the "directional" negative log FDR [sign of fold change * $-\log_{10}$(FDR)]. Ranked gene lists were composed of both the complete set of expressed genes passing the abovementioned expression threshold (total tags, or TT) and the subset of differential genes passing the abovementioned significance thresholds (significantly differential, or Sig). For GSEAs of mouse RNA-seq data, gene IDs were first converted using a human-to-mouse homolog table retrieved from Ensembl Biomart (Ensembl Genes 98). In the cases in which no homologous genes were found, the mouse IDs were simply converted to uppercase names.

For the GSEAs of STAT1-responsive genes (Supplementary Fig. S4J), four samples of fragments per kilobase per million mapped fragments (FPKM) expression data were retrieved from Gene Expression Omnibus (GEO) GSE98372 (55): GSM2592890_HepG2_UN_FPKM.txt.gz, GSM2592891_HepG2_IFNa_FPKM.txt.gz, GSM2592894_STAT1-KO_UN_FPKM.txt.gz, and GSM2592895_STAT1-KO_IFNa_FPKM.txt.gz. DE genes were determined between HepG2_UN and HepG2_IFNa ($\log_2$ fold change >1) and between STAT1-KO_UN and STAT1-KO_IFNa. The two DE lists were compared, and 111 genes were found to be DE upregulated between HepG2_UN and HepG2_IFNa and unchanged (not DE) between STAT1-KO_UN and STAT1-KO_IFNa. This 111-gene list was grouped and named GSE98372_DE_UP and used as a gene set collection for GSEA to represent STAT1-responsive genes.

Heat maps, box plots, and Venn diagrams were generated using custom Python and R scripts. Additionally, box plots and Venn diagrams were generated using BoxPlotR (108) and the Venn Webtool (http://bioinformatics.psb.ugent.be/webtools/Venn/), respectively.

For GSVA, we derived our gene sets from differential expression results comparing hexamer versus dodecamer signaling at day 2 (Fig. 5B), using significantly upregulated genes (logFC ≥1, FDR <0.05) as our hexamer signature and significantly downregulated genes as our dodecamer signature (logFC ≤ −1, FDR <0.05). We next applied GSVA with "Gaussian" kcdf to transcripts per kilobase million (TPM)–normalized gene expression data from TCGA (25),

Beat AML (26), and Leucegene (57). We also applied GSVA to quantile normalized microarray data from sorted AML fractions (ref. 20; GSE76008) as well as TPM-normalized RNA-seq from a subset of those AML fractions (32). This yielded a signature-specific enrichment score for each patient. We then took the difference between hexamer signature enrichment and dodecamer signature enrichment to derive a hexamer versus dodecamer score, which was then compared between LSC^+ and LSC^- fractions as well as different genomic subtypes within the cohorts. All comparisons were performed using a two-tailed unpaired *t* test. Data will be made available upon request.

To derive intersect hexamer and dodecamer signatures, we started with genes that were significantly DE between hexamer versus dodecamer signaling at day 2 (FDR <0.05, no logFC cutoff) and evaluated the correlation of these genes with the IL3Rα/βc surface protein ratio from 10 primary AMLs within the Toronto cohort for which we had both RNA-seq and immunophenotypic profiles. Among 394 DE genes enriched with enforced hexamer signaling, 34 genes were positively correlated with the IL3Rα/βc primary AML surface ratio at $P < 0.05$, comprising an "intersect hexamer signature." Among the 713 DE genes enriched with enforced dodecamer signaling, 41 genes were negatively correlated with the IL3Rα/βc primary AML surface ratio at $P < 0.05$, comprising an "intersect dodecamer signature." These intersect hexamer and dodecamer signatures were evaluated through the same approach as the differential expression–derived signatures.

Statistical Analyses

Unless otherwise stated, data are represented as mean ± SEM, and *P* values comparing means were calculated using a two-tailed unpaired Student *t* test, one-way or two-way ANOVA with *post hoc* test specified, or Mann–Whitney test in GraphPad Prism v.8.0.2 or v8.4.3 (RRID: SCR_002798) as indicated. A *P* value less than 0.05 was considered statistically significant.

Data and Material Availability and Correspondence

Atomic coordinates and structure factors of the IL3R ternary complex have been deposited in the PDB under the ID code 6NMY. RNA-seq data are available in the GEO database under accession number GSE141232. Data and materials relevant to this study are available from the corresponding authors upon reasonable request.

Authors' Disclosures

T.R. Hercus reports grants from Cancer Council SA during the conduct of the study. B.A. Benard reports grants from the Blavatnik Family Foundation during the conduct of the study. P.G. Ekert reports other support from Illumina and the Walter and Eliza Hall Institute outside the submitted work. J.E. Dick reports grants from Celgene/Bristol Myers Squibb and personal fees from Graphite Bio scientific advisory board outside the submitted work, as well as a patent for SIRP-alpha issued, licensed, and with royalties paid from Trillium Therapeutics/Pfizer. M.W. Parker reports grants from the National Health and Medical Reseach Council of Australia and the Cancer Council of Victoria during the conduct of the study. A.F. Lopez reports grants from the National Health and Medical Research Council of Australia and Cancer Council SA during the conduct of the study. No disclosures were reported by the other authors.

Authors' Contributions

W.L. Kan: Conceptualization, formal analysis, investigation, visualization, methodology, writing–original draft, writing–review and editing. **U. Dhagat:** Conceptualization, formal analysis, investigation, visualization, methodology, writing–original draft, writing–review and editing. **K.B. Kaufmann:** Conceptualization, formal analysis, investigation, visualization, methodology, writing–original draft, writing–review and editing. **T.R. Hercus:** Conceptualization, formal analysis, investigation, visualization, methodology, writing–original draft, writing–review and editing. **T.L. Nero:** Formal analysis, writing–original draft, writing–review and editing. **A.G.X. Zeng:** Formal analysis, investigation, visualization, methodology, writing–original draft, writing–review and editing. **J. Toubia:** Formal analysis, visualization, methodology. **E.F. Barry:** Formal analysis, investigation, visualization. **S.E. Broughton:** Formal analysis, visualization. **G.A. Gomez:** Formal analysis, investigation, visualization, methodology. **B.A. Benard:** Formal analysis. **M. Dottore:** Formal analysis, investigation. **K.S. Cheung Tung Shing:** Formal analysis, visualization. **H. Boutzen:** Formal analysis. **S.E. Samaraweera:** Formal analysis. **K.J. Simpson:** Formal analysis, investigation, methodology. **L. Jin:** Formal analysis. **G.J. Goodall:** Writing–review and editing. **C.G. Begley:** Formal analysis, writing–review and editing. **D. Thomas:** Formal analysis, writing–review and editing. **P.G. Ekert:** Formal analysis, writing–review and editing. **D. Tvorogov:** Formal analysis, investigation, visualization, writing–review and editing. **R.J. D'Andrea:** Formal analysis, visualization, writing–original draft, writing–review and editing. **J.E. Dick:** Conceptualization, resources, formal analysis, supervision, funding acquisition, visualization, methodology, writing–original draft, project administration, writing–review and editing. **M.W. Parker:** Conceptualization, resources, formal analysis, supervision, funding acquisition, visualization, methodology, writing–original draft, project administration, writing–review and editing. **A.F. Lopez:** Conceptualization, resources, formal analysis, supervision, funding acquisition, visualization, methodology, writing–original draft, project administration, writing–review and editing.

Acknowledgments

This research was undertaken in part using the MX2 beamline at the Australian Synchrotron, part of the Australian Nuclear Science and Technology Organisation (ANSTO), and made use of the Australian Cancer Research Foundation (ACRF) detector. We thank the beamline staff for their assistance, particularly Dr. Santosh Panjikar for his help with data processing. We thank Anna Sapa for technical assistance, Tony Cambareri for the 1B5 hybridoma, and Nic Nicola, Frank Stomski, and Amanda Mitchell for helpful discussions. We thank the South Australian Cancer Research Biobank (Adelaide, Australia), the Leukemia Tissue Bank at Princess Margaret Cancer Centre (Toronto, Ontario, Canada), and particularly Mark D. Minden, Andrea Arruda, and Amanda Mitchell for providing access to primary AML patient samples. We acknowledge the use of the CSIRO Collaborative Crystallization Centre (Melbourne, Australia) for our initial crystallization studies, the ACRF Rational Drug Discovery Centre (Fitzroy, Australia), and the ACRF Facility of Innovative Cancer Drug Discovery (Parkville, Australia). We also acknowledge the use of the ACRF Cancer Genomics Facility (J. Toubia) (Adelaide, Australia), the ACRF Cancer Discovery Accelerator Facility (Adelaide, Australia), and the Cytometry Facility at the Centre for Cancer Biology (Adelaide, Australia). We thank the ACRF (Cancer Discovery Accelerator) for funding the imaging equipment used in this work. We thank Arthi Macpherson from the Victorian Centre for Functional Genomics and the ACRF Translational Reverse Phase Protein Array platform at Peter MacCallum Cancer Centre for assistance with RPPA. This work was supported by grants from the National Health and Medical Research Council of Australia (NHMRC) to A.F. Lopez, M.W. Parker, and T. Hughes (APP1071897); to A.F. Lopez, D. Tvorogov, and D. Thomas (APP1182564); to A.F. Lopez, W.L. Kan, R.J. D'Andrea, S.E. Samaraweera, J.E. Dick, D. Ross, and C.G. Begley (APP2021560); Cancer Council SA Beat Cancer Fund to T.R. Hercus and A.F. Lopez (APP1148221); Cancer Council Victoria to U. Dhagat, S.E. Broughton, M.W. Parker, and L. Purton (APP1123401); Cure Cancer Australia to S.E. Broughton (APP1098567); and ACRF to M.W. Parker. Funding from the Victorian Government Operational Infrastructure Support Scheme to St Vincent's Institute is acknowledged. S.E. Broughton was

supported by a Leukemia Foundation Fellowship, and M.W. Parker is an NHMRC Research Fellow (APP1117183) and an NHMRC Investigator (APP1194263). The Victorian Centre for Functional Genomics (K.J. Simpson) is funded by the ACRF, the Australian Phenomics Network through funding from the Australian Government's National Collaborative Research Infrastructure Strategy program, the Peter MacCallum Cancer Centre Foundation, and the University of Melbourne Research Collaborative Infrastructure Program. J.E. Dick is supported by funds from the Princess Margaret Cancer Centre Foundation, Ontario Institute for Cancer Research through funding provided by the Government of Ontario, Canadian Institutes for Health Research grants 130412, 89932, and 154293, International Development Research Centre Ottawa Canada grants 108401 and 109153, Canadian Cancer Society grant 703212, Terry Fox New Frontiers Program Project Grant 1047, the University of Toronto's Medicine by Design initiative with funding from the Canada First Research Excellence Fund, and a Canada Research Chair.

The publication costs of this article were defrayed in part by the payment of publication fees. Therefore, and solely to indicate this fact, this article is hereby marked "advertisement" in accordance with 18 USC section 1734.

Note

Supplementary data for this article are available at Cancer Discovery Online (http://cancerdiscovery.aacrjournals.org/).

Received December 13, 2022; revised April 6, 2023; accepted May 12, 2023; published first May 16, 2023.

REFERENCES

1. Lapidot T, Sirard C, Vormoor J, Murdoch B, Hoang T, Caceres-Cortes J, et al. A cell initiating human acute myeloid leukaemia after transplantation into SCID mice. Nature 1994;367:645–8.
2. Bonnet D, Dick JE. Human acute myeloid leukemia is organized as a hierachy that originates from a primitive hematopoietic cell. Nat Med 1997;3:730–7.
3. Kan WL, Cheung Tung Shing KS, Nero TL, Hercus TR, Tvorogov D, Parker MW, et al. Messing with βc: a unique receptor with many goals. Semin Immunol 2021;54:101513.
4. Spangler JB, Moraga I, Mendoza JL, Garcia KC. Insights into cytokine-receptor interactions from cytokine engineering. Annu Rev Immunol 2015;33:139–67.
5. Gorby C, Martinez-Fabregas J, Wilmes S, Moraga I. Mapping determinants of cytokine signaling via protein engineering. Front Immunol 2018;9:2143.
6. Mohan K, Ueda G, Kim AR, Jude KM, Fallas JA, Guo Y, et al. Topological control of cytokine receptor signaling induces differential effects in hematopoiesis. Science 2019;364:eaav7532.
7. Moraga I, Spangler J, Mendoza JL, Garcia KC. Multifarious determinants of cytokine receptor signaling specificity. Adv Immunol 2014;121:1–39.
8. Ho CCM, Chhabra A, Starkl P, Schnorr PJ, Wilmes S, Moraga I, et al. Decoupling the functional pleiotropy of stem cell factor by tuning c-Kit signaling. Cell 2017;168:1041–52.
9. Mo F, Yu Z, Li P, Oh J, Spolski R, Zhao L, et al. An engineered IL-2 partial agonist promotes CD8(+) T cell stemness. Nature 2021;597:544–8.
10. Mitra S, Ring AM, Amarnath S, Spangler JB, Li P, Ju W, et al. Interleukin-2 activity can be fine tuned with engineered receptor signaling clamps. Immunity 2015;42:826–38.
11. Mendoza JL, Escalante NK, Jude KM, Sotolongo Bellon J, Su L, Horton TM, et al. Structure of the IFNgamma receptor complex guides design of biased agonists. Nature 2019;567:56–60.
12. Spigel D, Spira A, Zamarin D, McDermott DF, Luke J, Heymach JV, et al. A phase 1a/1b study of STK-012, an α/β IL-2 receptor selective partial agonist as monotherapy and in combination with pembrolizumab in advanced solid tumors (NCT05098132) [abstract]. 2022; Philadelphia (PA). Proceedings of the American Association for Cancer Research Annual Meeting 2022; 2022 Apr 8–13. Philadelphia (PA): AACR. Cancer Res 82(12_Suppl): Abstract nr CT244.
13. Hansen G, Hercus TR, McClure BJ, Stomski FC, Dottore M, Powell J, et al. The structure of the GM-CSF receptor complex reveals a distinct mode of cytokine receptor activation. Cell 2008;134:496–507.
14. Sedek M, van der Velden LM, Strous GJ. Multimeric growth hormone receptor complexes serve as signaling platforms. J Biol Chem 2014;289:65–73.
15. Hercus TR, Kan WLT, Broughton SE, Tvorogov D, Ramshaw HS, Sandow JJ, et al. Role of the beta common (βc) family of cytokines in health and disease. Cold Spring Harb Perspect Biol 2018;10:39–64.
16. Jordan CT, Upchurch D, Szilvassy SJ, Guzman ML, Howard DS, Pettigrew AL, et al. The interleukin-3 receptor alpha chain is a unique marker for human acute myelogenous leukemia stem cells. Leukemia 2000;14:1777–84.
17. Jin L, Lee EM, Ramshaw HS, Busfield SJ, Peoppl AG, Wilkinson L, et al. Monoclonal antibody-mediated targeting of CD123, IL-3 receptor alpha chain, eliminates human acute myeloid leukemic stem cells. Cell stem cell 2009;5:31–42.
18. Testa U, Riccioni R, Militi S, Coccia E, Stellacci E, Samoggia P, et al. Elevated expression of IL-3Ralpha in acute myelogenous leukemia is associated with enhanced blast proliferation, increased cellularity, and poor prognosis. Blood 2002;100:2980–8.
19. Vergez F, Green AS, Tamburini J, Sarry JE, Gaillard B, Cornillet-Lefebvre P, et al. High levels of CD34+CD38low/-CD123+ blasts are predictive of an adverse outcome in acute myeloid leukemia: a Groupe Ouest-Est des Leucemies Aigues et Maladies du Sang (GOELAMS) study. Haematologica 2011;96:1792–8.
20. Ng SW, Mitchell A, Kennedy JA, Chen WC, McLeod J, Ibrahimova N, et al. A 17-gene stemness score for rapid determination of risk in acute leukaemia. Nature 2016;540:433–7.
21. Shlush LI, Mitchell A, Heisler L, Abelson S, Ng SWK, Trotman-Grant A, et al. Tracing the origins of relapse in acute myeloid leukaemia to stem cells. Nature 2017;547:104–8.
22. Libermann TA, Nusbaum HR, Razon N, Kris R, Lax I, Soreq H, et al. Amplification, enhanced expression and possible rearrangement of EGF receptor gene in primary human brain tumours of glial origin. Nature 1985;313:144–7.
23. Broughton SE, Dhagat U, Hercus TR, Nero TL, Grimbaldeston MA, Bonder CS, et al. The GM-CSF/IL-3/IL-5 cytokine receptor family: from ligand recognition to initiation of signaling. Immunol Rev 2012;250:277–302.
24. Slamon DJ, Godolphin W, Jones LA, Holt JA, Wong SG, Keith DE, et al. Studies of the HER-2/neu proto-oncogene in human breast and ovarian cancer. Science 1989;244:707–12.
25. Cancer Genome Atlas Research Network; Ley TJ, Miller C, Ding L, Raphael BJ, Mungall AJ, et al. Genomic and epigenomic landscapes of adult de novo acute myeloid leukemia. N Engl J Med 2013;368:2059–74.
26. Tyner JW, Tognon CE, Bottomly D, Wilmot B, Kurtz SE, Savage SL, et al. Functional genomic landscape of acute myeloid leukaemia. Nature 2018;562:526–31.
27. Verhaak RG, Wouters BJ, Erpelinck CA, Abbas S, Beverloo HB, Lugthart S, et al. Prediction of molecular subtypes in acute myeloid leukemia based on gene expression profiling. Haematologica 2009;94:131–4.
28. Metzeler KH, Hummel M, Bloomfield CD, Spiekermann K, Braess J, Sauerland MC, et al. An 86-probe-set gene-expression signature predicts survival in cytogenetically normal acute myeloid leukemia. Blood 2008;112:4193–201.
29. Bill M, Nicolet D, Kohlschmidt J, Walker CJ, Mrozek K, Eisfeld AK, et al. Mutations associated with a 17-gene leukemia stem cell score and the score's prognostic relevance in the context of the European LeukemiaNet classification of acute myeloid leukemia. Haematologica 2020;105:721–9.
30. Daver N, Schlenk RF, Russell NH, Levis MJ. Targeting FLT3 mutations in AML: review of current knowledge and evidence. Leukemia 2019;33:299–312.

31. Bottomly D, Long N, Schultz AR, Kurtz SE, Tognon CE, Johnson K, et al. Integrative analysis of drug response and clinical outcome in acute myeloid leukemia. Cancer Cell 2022;40:850–64.
32. Zeng AGX, Bansal S, Jin L, Mitchell A, Chen WC, Abbas HA, et al. A cellular hierarchy framework for understanding heterogeneity and predicting drug response in acute myeloid leukemia. Nat Med 2022; 28:1212–23.
33. Neubauer A, Maharry K, Mrozek K, Thiede C, Marcucci G, Paschka P, et al. Patients with acute myeloid leukemia and RAS mutations benefit most from postremission high-dose cytarabine: a Cancer and Leukemia Group B study. J Clin Oncol 2008;26:4603–9.
34. Eppert K, Takenaka K, Lechman ER, Waldron L, Nilsson B, van Galen P, et al. Stem cell gene expression programs influence clinical outcome in human leukemia. Nat Med 2011;17:1086–93.
35. van Galen P, Hovestadt V, Wadsworth Ii MH, Hughes TK, Griffin GK, Battaglia S, et al. Single-cell RNA-seq reveals AML hierarchies relevant to disease progression and immunity. Cell 2019;176:1265–81.
36. Xie SZ, Garcia-Prat L, Voisin V, Ferrari R, Gan OI, Wagenblast E, et al. Sphingolipid modulation activates proteostasis programs to govern human hematopoietic stem cell self-renewal. Cell stem cell 2019;25:639–53.
37. Xie SZ, Kaufmann KB, Wang W, Chan-Seng-Yue M, Gan OI, Laurenti E, et al. Sphingosine-1-phosphate receptor 3 potentiates inflammatory programs in normal and leukemia stem cells to promote differentiation. Blood Cancer Discov 2021;2:32–53.
38. Kaufmann KB, Garcia-Prat L, Liu Q, Ng SWK, Takayanagi SI, Mitchell A, et al. A stemness screen reveals C3orf54/INKA1 as a promoter of human leukemia stem cell latency. Blood 2019;133:2198–211.
39. Pabst C, Bergeron A, Lavallee VP, Yeh J, Gendron P, Norddahl GL, et al. GPR56 identifies primary human acute myeloid leukemia cells with high repopulating potential in vivo. Blood 2016;127: 2018–27.
40. Broughton SE, Hercus TR, Nero TL, Dottore M, McClure BJ, Dhagat U, et al. Conformational changes in the GM-CSF receptor suggest a molecular mechanism for affinity conversion and receptor signaling. Structure 2016;24:1271–81.
41. Tvorogov D, Thomas D, Liau NPD, Dottore M, Barry EF, Lathi M, et al. Accumulation of JAK activation loop phosphorylation is linked to type I JAK inhibitor withdrawal syndrome in myelofibrosis. Sci Adv 2018;4:eaat3834.
42. Brooks AJ, Dai W, O'Mara ML, Abankwa D, Chhabra Y, Pelekanos RA, et al. Mechanism of activation of protein kinase JAK2 by the growth hormone receptor. Science 2014;344:1249783.
43. Ferrari ML, Gomez GA, Maccioni HJ. Spatial organization and stoichiometry of N-terminal domain-mediated glycosyltransferase complexes in Golgi membranes determined by fret microscopy. Neurochem Res 2012;37:1325–34.
44. Gomez GA, McLachlan RW, Wu SK, Caldwell BJ, Moussa E, Verma S, et al. An RPTPalpha/Src family kinase/Rap1 signaling module recruits myosin IIB to support contractile tension at apical E-cadherin junctions. Mol Biol Cell 2015;26:1249–62.
45. Brumatti G, Salmanidis M, Kok CH, Bilardi RA, Sandow JJ, Silke N, et al. HoxA9 regulated Bcl-2 expression mediates survival of myeloid progenitors and the severity of HoxA9-dependent leukemia. Oncotarget 2013;4:1933–47.
46. Wang GG, Calvo KR, Pasillas MP, Sykes DB, Hacker H, Kamps MP. Quantitative production of macrophages or neutrophils ex vivo using conditional Hoxb8. Nat Methods 2006;3:287–93.
47. Broughton SE, Hercus TR, Nero TL, Kan WL, Barry EF, Dottore M, et al. A dual role for the N-terminal domain of the IL-3 receptor in cell signalling. Nat Commun 2018;9:386.
48. Ivanova NB, Dimos JT, Schaniel C, Hackney JA, Moore KA, Lemischka IR. A stem cell molecular signature. Science 2002;298:601–4.
49. Ramshaw HS, Guthridge MA, Stomski FC, Barry EF, Ooms L, Mitchell CA, et al. The Shc-binding site of the βc subunit of the GM-CSF/IL-3/IL-5 receptors is a negative regulator of hematopoiesis. Blood 2007;110:3582–90.
50. Coccia EM, Del Russo N, Stellacci E, Testa U, Marziali G, Battistini A. STAT1 activation during monocyte to macrophage maturation: role of adhesion molecules. Int Immunol 1999;11:1075–83.
51. Jerke U, Tkachuk S, Kiyan J, Stepanova V, Kusch A, Hinz M, et al. Stat1 nuclear translocation by nucleolin upon monocyte differentiation. PLoS One 2009;4:e8302.
52. van Galen P, Kreso A, Mbong N, Kent DG, Fitzmaurice T, Chambers JE, et al. The unfolded protein response governs integrity of the haematopoietic stem-cell pool during stress. Nature 2014;510: 268–72.
53. Brown AL, Salerno DG, Sadras T, Engler GA, Kok CH, Wilkinson CR, et al. The GM-CSF receptor utilizes beta-catenin and Tcf4 to specify macrophage lineage differentiation. Differentiation 2012;83:47–59.
54. Nelson RK, Brickner H, Panwar B, Ramirez-Suastegui C, Herrera-de la Mata S, Liu N, et al. Human eosinophils express a distinct gene expression program in response to IL-3 compared with common beta-chain cytokines IL-5 and GM-CSF. J Immunol 2019;203:329–37.
55. Chen K, Liu J, Liu S, Xia M, Zhang X, Han D, et al. Methyltransferase SETD2-mediated methylation of STAT1 is critical for interferon antiviral activity. Cell 2017;170:492–506.
56. Wu X, Dao Thi VL, Huang Y, Billerbeck E, Saha D, Hoffmann HH, et al. Intrinsic immunity shapes viral resistance of stem cells. Cell 2018;172:423–38.
57. Simon L, Lavallee VP, Bordeleau ME, Krosl J, Baccelli I, Boucher G, et al. Chemogenomic landscape of RUNX1-mutated AML reveals importance of RUNX1 allele dosage in genetics and glucocorticoid sensitivity. Clin Cancer Res 2017;23:6969–81.
58. Assi SA, Imperato MR, Coleman DJL, Pickin A, Potluri S, Ptasinska A, et al. Subtype-specific regulatory network rewiring in acute myeloid leukemia. Nat Genet 2019;51:151–62.
59. Goedhart J, van Weeren L, Adjobo-Hermans MJ, Elzenaar I, Hink MA, Gadella TW Jr. Quantitative co-expression of proteins at the single cell level–application to a multimeric FRET sensor. PLoS One 2011; 6:e27321.
60. Boutzen H, Madani Tonekaboni SA, Chan-Seng-Yue M, Murison A, Takayama N, Mbong N, et al. A primary hierarchically organized patient-derived model enables in depth interrogation of stemness driven by the coding and non-coding genome. Leukemia 2022;36: 2690–704.
61. Kaufmann KB, Zeng AGX, Coyaud E, Garcia-Prat L, Papalexi E, Murison A, et al. A latent subset of human hematopoietic stem cells resists regenerative stress to preserve stemness. Nat Immunol 2021; 22:723–34.
62. Lechman ER, Gentner B, Ng SW, Schoof EM, van Galen P, Kennedy JA, et al. miR-126 regulates distinct self-renewal outcomes in normal and malignant hematopoietic stem cells. Cancer Cell 2016;29:214–28.
63. Surka C, Jin L, Mbong N, Lu CC, Jang IS, Rychak E, et al. CC-90009, a novel cereblon E3 ligase modulator, targets acute myeloid leukemia blasts and leukemia stem cells. Blood 2021;137:661–77.
64. Ho TC, LaMere M, Stevens BM, Ashton JM, Myers JR, O'Dwyer KM, et al. Evolution of acute myelogenous leukemia stem cell properties after treatment and progression. Blood 2016;128:1671–8.
65. Fatrai S, Wierenga AT, Daenen SM, Vellenga E, Schuringa JJ. Identification of HIF2alpha as an important STAT5 target gene in human hematopoietic stem cells. Blood 2011;117:3320–30.
66. Schepers H, Wierenga AT, Vellenga E, Schuringa JJ. STAT5-mediated self-renewal of normal hematopoietic and leukemic stem cells. JAKSTAT 2012;1:13–22.
67. Wang Z, Li G, Tse W, Bunting KD. Conditional deletion of STAT5 in adult mouse hematopoietic stem cells causes loss of quiescence and permits efficient nonablative stem cell replacement. Blood 2009;113:4856–65.
68. Moriggl R, Sexl V, Kenner L, Duntsch C, Stangl K, Gingras S, et al. Stat5 tetramer formation is associated with leukemogenesis. Cancer Cell 2005;7:87–99.
69. Schuringa JJ, Chung KY, Morrone G, Moore MA. Constitutive activation of STAT5A promotes human hematopoietic stem cell self-renewal and erythroid differentiation. J Exp Med 2004;200:623–35.
70. Wierenga AT, Vellenga E, Schuringa JJ. Maximal STAT5-induced proliferation and self-renewal at intermediate STAT5 activity levels. Mol Cell Biol 2008;28:6668–80.
71. Cui L, Moraga I, Lerbs T, Van Neste C, Wilmes S, Tsutsumi N, et al. Tuning MPL signaling to influence hematopoietic stem cell

differentiation and inhibit essential thrombocythemia progenitors. Proc Natl Acad Sci U S A 2021;118:e2017849118.
72. Chen E, Beer PA, Godfrey AL, Ortmann CA, Li J, Costa-Pereira AP, et al. Distinct clinical phenotypes associated with JAK2V617F reflect differential STAT1 signaling. Cancer Cell 2010;18:524–35.
73. Vergez F, Largeaud L, Bertoli S, Nicolau ML, Rieu JB, Vergnolle I, et al. Phenotypically-defined stages of leukemia arrest predict main driver mutations subgroups, and outcome in acute myeloid leukemia. Blood Cancer J 2022;12:117.
74. Saxton RA, Tsutsumi N, Su LL, Abhiraman GC, Mohan K, Henneberg LT, et al. Structure-based decoupling of the pro- and anti-inflammatory functions of interleukin-10. Science 2021;371:eabc8433.
75. Silva DA, Yu S, Ulge UY, Spangler JB, Jude KM, Labao-Almeida C, et al. De novo design of potent and selective mimics of IL-2 and IL-15. Nature 2019;565:186–91.
76. Scott CL, Robb L, Papaevangeliou B, Mansfield R, Nicola NA, Begley CG. Reassessment of interactions between hematopoietic receptors using common beta-chain and interleukin-3-specific receptor beta-chain-null cells: no evidence of functional interactions with receptors for erythropoietin, granulocyte colony-stimulating factor, or stem cell factor. Blood 2000;96:1588–90.
77. Lun AT, Bach K, Marioni JC. Pooling across cells to normalize single-cell RNA sequencing data with many zero counts. Genome Biol 2016;17:75.
78. Broughton SE, Hercus TR, Nero TL, Dhagat U, Owczarek CM, Hardy MP, et al. Crystallization and preliminary X-ray diffraction analysis of the interleukin-3 alpha receptor bound to the Fab fragment of antibody CSL362. Acta Crystallogr F Struct Biol Commun 2014;70(Pt 3):358–61.
79. McClure BJ, Hercus TR, Cambareri BA, Woodcock JM, Bagley CJ, Howlett GJ, et al. Molecular assembly of the ternary granulocyte-macrophage colony-stimulating factor receptor complex. Blood 2003;101:1308–15.
80. Hercus TR, Barry EF, Dottore M, McClure BJ, Webb AI, Lopez AF, et al. High yield production of a soluble human interleukin-3 variant from E. coli with wild-type bioactivity and improved radiolabeling properties. PLoS One 2013;8:e74376.
81. Aragao D, Aishima J, Cherukuvada H, Clarken R, Clift M, Cowieson NP, et al. MX2: a high-flux undulator microfocus beamline serving both the chemical and macromolecular crystallography communities at the Australian Synchrotron. J Synchrotron Radiat 2018;25(Pt 3):885–91.
82. McPhillips TM, McPhillips SE, Chiu HJ, Cohen AE, Deacon AM, Ellis PJ, et al. Blu-Ice and the distributed control system: software for data acquisition and instrument control at macromolecular crystallography beamlines. J Synchrotron Radiat 2002;9(Pt 6):401–6.
83. Kabsch W. Xds. Acta Crystallogr D Biol Crystallog 2010;66(Pt 2):125–32.
84. Evans PR, Murshudov GN. How good are my data and what is the resolution? Acta Crystallogr D Biol Crystallogr 2013;69(Pt 7):1204–14.
85. McCoy AJ, Grosse-Kunstleve RW, Adams PD, Winn MD, Storoni LC, Read RJ. Phaser crystallographic software. J Appl Crystallogr 2007;40(Pt 4):658–74.
86. Feng Y, Klein BK, McWherter CA. Three-dimensional solution structure and backbone dynamics of a variant of human interleukin-3. J Mol Biol 1996;259:524–41.
87. Emsley P, Cowtan K. Coot: model-building tools for molecular graphics. Acta Crystallogr D Biol Crystallogr 2004;60(Pt 12 Pt 1):2126–32.
88. Murshudov GN, Vagin AA, Dodson EJ. Refinement of macromolecular structures by the maximum-likelihood method. Acta Crystallogr D Biol Crystallogr 1997;53(Pt 3):240–55.
89. Barry SC, Bagley CJ, Phillips J, Dottore M, Cambareri B, Moretti P, et al. Two contiguous residues in human interleukin-3, Asp^{21} and Glu^{22}, selectively interact with the α- and β-chains of its receptor and participate in function. J Biol Chem 1994;269:8488–92.
90. Woodcock JM, Bagley CJ, Zacharakis B, Lopez AF. A single tyrosine residue in the membrane-proximal domain of the GM-CSF, IL-3 and IL-5 receptor common β chain is necessary and sufficient for high-affinity binding and signalling by all three ligands. J Biol Chem 1996;271:25999–6006.
91. Hercus TR, Thomas D, Guthridge MA, Ekert PG, King-Scott J, Parker MW, et al. The granulocyte-macrophage colony-stimulating factor receptor: linking its structure to cell signaling and its role in disease. Blood 2009;114:1289–98.
92. Bindels DS, Haarbosch L, van Weeren L, Postma M, Wiese KE, Mastop M, et al. mScarlet: a bright monomeric red fluorescent protein for cellular imaging. Nat Methods 2017;14:53–6.
93. Jares-Erijman EA, Jovin TM. FRET imaging. Nat Biotechnol 2003;21:1387–95.
94. Broughton SE, Hercus TR, Hardy MP, McClure BJ, Nero TL, Dottore M, et al. Dual mechanism of interleukin-3 receptor blockade by an anti-cancer antibody. Cell Rep 2014;8:410–9.
95. Munson PJ, Rodbard D. Ligand - a versatile computerized approach for characterization of ligand-binding systems. Anal Biochem 1980;107:220–39.
96. Persons DA, Mehaffey MG, Kaleko M, Nienhuis AW, Vanin EF. An improved method for generating retroviral producer clones for vectors lacking a selectable marker gene. Blood Cells Mol Dis 1998;24:167–82.
97. Stomski FC, Sun Q, Bagley CJ, Woodcock JM, Goodall GJ, Andrews RK, et al. Human interleukin-3 (IL-3) induces disulphide-linked receptor α and β chain heterodimerization which is required for receptor activation but not high affinity binding. Mol Cell Biol 1996;16:3035–46.
98. Sun Q, Woodcock JM, Rapoport A, Stomski FC, Korpelainen EI, Bagley CJ, et al. Monoclonal antibody 7G3 recognizes the *N*-terminal domain of the human interleukin-3 (IL-3) receptor α-chain and functions as a specific IL-3 receptor antagonist. Blood 1996;87:83–92.
99. Hu Y, Smyth GK. ELDA: extreme limiting dilution analysis for comparing depleted and enriched populations in stem cell and other assays. J Immunol Methods 2009;347:70–8.
100. Dobin A, Davis CA, Schlesinger F, Drenkow J, Zaleski C, Jha S, et al. STAR: ultrafast universal RNA-seq aligner. Bioinformatics 2013;29:15–21.
101. Thorvaldsdottir H, Robinson JT, Mesirov JP. Integrative Genomics Viewer (IGV): high-performance genomics data visualization and exploration. Brief Bioinform 2013;14:178–92.
102. Robinson MD, McCarthy DJ, Smyth GK. edgeR: a Bioconductor package for differential expression analysis of digital gene expression data. Bioinformatics 2010;26:139–40.
103. Lun AT, Chen Y, Smyth GK. It's DE-licious: a recipe for differential expression analyses of RNA-seq experiments using quasi-likelihood methods in edgeR. Methods Mol Biol 2016;1418:391–416.
104. Su S, Law CW, Ah-Cann C, Asselin-Labat ML, Blewitt ME, Ritchie ME. Glimma: interactive graphics for gene expression analysis. Bioinformatics 2017;33:2050–2.
105. Huang da W, Sherman BT, Lempicki RA. Bioinformatics enrichment tools: paths toward the comprehensive functional analysis of large gene lists. Nucleic Acids Res 2009;37:1–13.
106. Mootha VK, Lindgren CM, Eriksson KF, Subramanian A, Sihag S, Lehar J, et al. PGC-1alpha-responsive genes involved in oxidative phosphorylation are coordinately downregulated in human diabetes. Nat Genet 2003;34:267–73.
107. Subramanian A, Tamayo P, Mootha VK, Mukherjee S, Ebert BL, Gillette MA, et al. Gene set enrichment analysis: a knowledge-based approach for interpreting genome-wide expression profiles. Proc Natl Acad Sci U S A 2005;102:15545–50.
108. Spitzer M, Wildenhain J, Rappsilber J, Tyers M. BoxPlotR: a web tool for generation of box plots. Nat Methods 2014;11:121–2.